Department of Physics and Astronomy

Heidelberg University

Master thesis

in Physics

submitted by

Alexander Flamm

born in Bad Urach

2025

Novel readout sequences and local control for spinor Bose-Einstein condensates

This Master thesis has been carried out by Alexander Flamm

at the

Kirchhoff-Institute for Physics

under the supervision of

Prof. Dr. Markus K. Oberthaler

Novel readout sequences and local control for spinor Bose-Einstein condensates:

Recently, ferromagnetic spinor Bose-Einstein condensates were proposed by Siovitz et al. [37] as a platform for studying the sine-Gordon equation as a relativistic field theory, where the relevant degree of freedom is the spinor phase. In the first part, this thesis describes two new readout sequences for simultaneous measurement of non-commuting spin observables, expanding on the work of Kunkel et al. [22]. The sequences are further applied to characterize sine-Gordon solitons in a single shot, thereby reducing the necessary measurement time. This reduces the effect of experimental drifts. Also a breathing solution could be measured, which covers the entire spin-nematic sphere. In the second part, a setup for localized hyperfine transitions was tested on the condensate, which had previously been constructed as part of a bachelor's thesis from Suelberg [42]. In the pseudospin-1/2 system between $|F = 1, m_\mathrm{F} = 0\rangle$ and $|F = 2, m_\mathrm{F} = 0\rangle$, dark-bright solitons could be generated, whose time evolution could be studied up to 500 ms including reflection at the potential wall.

Neue Auslesesequenzen und lokale Kontrolle für Spinor Bose-Einstein Kondensate:

Kürzlich wurden von Siovitz et al. [37] ferromagnetische Spinor Bose-Einstein Kondensate als Plattform für die Untersuchung der Sine-Gordon Gleichung als relativistische Feldtheorie vorgestellt, wobei die Spinorphase der relevante Freiheitsgrad ist. Im ersten Teil werden zwei neue Auslesesequenzen für die gleichzeitige Messung nichtkommutierender Spinobservablen beschrieben, die auf der Arbeit von Kunkel et al. [22] aufbauen. Die Sequenzen werden weiter angewendet, um sine-Gordon Solitonen in Einzelschuss zu charakterisieren, wodurch die nötige Messdauer verkürzt wird. Dies reduziert den Effekt von experimentellen Drifts. Außerdem konnte ein Breather gemessen werden, der den gesamten Spinnematischen Raum einnimmt. Im zweiten Teil wurde ein Aufbau für lokalisierte Hyperfeinübergänge am Kondensat getestet, der zuvor im Rahmen einer Bachelorarbeit von Suelberg [42] gebaut worden war. Im Pseudospin-1/2 System zwischen $|F = 1, m_\mathrm{F} = 0\rangle$ und $|F = 2, m_\mathrm{F} = 0\rangle$ konnten dunkle und helle Solitonen erzeugt werden, deren Zeitentwicklung bis zu 500 ms einschließlich der Reflektion am Wandpotential untersucht wurde.

Contents

0.1 List of Figures

Acronyms

AWG arbitrary waveform generator. 25

BEC Bose-Einstein condensate. 1–4, 12, 19, 20, 23, 28, 29, 32, 33, 36

DSG double sine-Gordon. 1, 17

DuPR dual-phase readout. 8, 9, 30, 36, 40

EOM electro-optical modulator. 23

EP easy-plane. 4, 5, 15, 16, 27, 29

GPE Gross-Pitaevskii equation. 3, 13, 15, 17, 32

KG Klein-Gordon. 1, 16

LEEFT low-energy effective field theory. 3, 17, 29

MW microwave. 1, 8, 12, 13, 19, 20, 23, 25–27, 30, 33, 35–37

POVM Positive Operator-Valued Measure. 7–11

RF radiofrequency. 8, 10, 19, 20, 22, 25, 26

SCC spin-changing collisions. 12

sG sine-Gordon. iii, 1–4, 11, 16–18, 20, 23, 25, 28–31, 36

WG waveguide. 19, 20

XDT crossed dipole trap. 19, 20, 27

1 Introduction

Atomic gases provide a unique opportunity to probe quantum dynamics far from equilibrium, as well as scrutinize magnetic domains in situ. Rubidium has, as an example for spinor Bose-Einstein condensates, non-zero internal angular momentum, which enables superfluidity and magnetism simultaneously. In magnetism, the boundaries between magnetic domains are of great interest, especially one specific domain wall, which is creating a solitary wave [44, 43]. A soliton is a non-dispersive, shape maintaining wave packet through the counterplay between dispersion and nonlinear interaction, arising in multiple nonlinear systems, such as in water, molecular biology, astrophysics, optical systems, and in weather phenomena [1, 36]. A specific soliton has recently become of particular interest to the group's research, which is a solution of the sine-Gordon (sG) equation, a nonlinear variant of the Klein-Gordon (KG) equation. The sG model is of high importance in the field of nonlinear wave dynamics [17], as it is a prototypical integrable model with propagating solitonic solutions. This can not only capture the dynamical behavior of a variety of physical systems such as Josephson-junctions and spin waves in magnetic materials [5], but is furthermore also of mathematical relevance, for example on surfaces with constant negative curvature [26]. The sG soliton was found as a solution to the sG equation, which - since the model is integrable - can be solved analytically and was studied numerically to great detail [5, 3, 20].

It was recently shown by Siovitz et al. [37], that a rubidium-87 Bose-Einstein condensate (BEC) can be described in the low energy limit as a double sine-Gordon (DSG) model. It can therefore serve as a platform to study the dynamics of solitonic excitations in this scalar relativistic field theory. During these studies, the characteristics of the sG solitons such as the propagation velocity and collision behavior could be extracted well in the relevant degrees of freedom, which are the spinor phase and the Larmor phase. But the readout was only possible in separate measurements. This is due to the composition of the non-commuting observables in the spin-1 system, which are based on the work of Kunkel et al. [22]. Expanding the previous readout sequences by fully utilizing the $F = 2$ manifold in rubidium-87 enables, firstly, to investigate the temporal connection between the events and, secondly, to capture the dynamics in a single run. This is beneficial in reducing the impact of experimental drifts by shortening the duration of the experiment.

In the first part, the aim of this thesis is the development and verification of two new readout sequences to support the project [7]. Additionally, a second project proposed a direct imprint technique using a microwave-modulated light beam. For this application, a setup was created as part of a bachelor's thesis [42], which is implemented and tested on the condensate.

This thesis is structured as follows: Chapter 2 covers the theory of the spin-1 system. This includes the theoretical foundations of the new readout sequences and the interaction between the atoms. Also the sine-Gordon model is introduced. Chapter 3 is about the experimental setup, from the Bose-Einstein condensate to the preparation of the initial states and the imaging. Chapter 4 reports on the measurement results. The stability of the magnetic field as well as the characterization of the local imprint are discussed before the results are presented using the new readout tools. Chapter 5 summarizes the outcomes and provides an outlook on the individual parts.

2 Theory

The rubidium-87 spinor Bose-Einstein condensate (BEC) offers an exceptional platform to study non-equilibrium many-body physics. In order to understand the spin-1 system, first the operators are introduced on a single-particle level, which builds the theoretical foundation for the development of the new readout sequences. Then, the condensate is described on a mean-field level through the Gross-Pitaevskii equation (GPE), before the interaction can be reduced to a low-energy effective field theory (LEEFT). Therefore, the sine-Gordon (sG) model is introduced to provide the necessary understanding for the dynamics of the system in this regime.

2.1 Spin-1 rubidium-87

The hydrogenlike ^{87}Rb has 37 electrons, thus the electronic configuration is [Kr]1s, with the ground state being $5^2\mathrm{S}_{1/2}$. The nucleus has nuclear spin $I = 3/2$, adding up with the electron spin in total to two hyperfine states $F = 1$ and $F = 2$ [40]. In the experiment, dynamics are usually studied in the $F = 1$ spin-1 manifold with the Zeeman levels $m_F \in \{-1, 0, 1\}$, but the $F = 2$ levels are used for complex readout schemes, described further in Section 2.5. On the single particle level, an arbitrary pure state $|\Psi\rangle$ can be expressed as a superposition of the three substates $|m_\mathrm{F}\rangle$ and their respective probability amplitudes p_i, where $\sum_i p_i^2 = 1$ holds:

$$|\Psi\rangle = \sum_{i\in\{-1,0,+1\}} p_i \mathrm{e}^{\varphi_i} |m_i\rangle \tag{2.1}$$

$$= \mathrm{e}^{i\varphi_g}\Big(p_{+1}\mathrm{e}^{i\varphi_\mathrm{L}} |m_{+1}\rangle + p_0\mathrm{e}^{i\varphi_\mathrm{S}} |m_0\rangle + p_{-1}\mathrm{e}^{-i\varphi_\mathrm{L}} |m_{-1}\rangle\Big) . \tag{2.2}$$

The Larmor phase is defined as $\varphi_\mathrm{L} = \varphi_1 - \varphi_{-1}$ and the spinor phase as $\varphi_\mathrm{S} = \varphi_0 - (\varphi_1 + \varphi_{-1})/2$. With three available states, the spin system builds an $\mathfrak{su}(3)$ algebra spanned by eight generators, e.g., the Gell-Mann matrices [10]. For the experimental system, however, it is more suitable to use different matrices. These operators are now subsequently introduced: Three of them can be organized in different $\mathfrak{su}(2)$ subspaces on spheres similar to the Bloch sphere in a spin-1/2 system. There is the spin-1 sphere or magnetization with the operators $\{\hat{\mathcal{F}}_x, \hat{\mathcal{F}}_y, \hat{\mathcal{F}}_z\}$, which fulfill the commutation relation $[\hat{\mathcal{F}}_i, \hat{\mathcal{F}}_j] = \mathrm{i}\epsilon_{ijk}\hat{\mathcal{F}}_k$ with $i, j \in \{x, y, z\}$ [12]:

$$\hat{\mathcal{F}}_x = \frac{1}{\sqrt{2}}\begin{pmatrix} 0 & 1 & 0 \\ 1 & 0 & 1 \\ 0 & 1 & 0 \end{pmatrix}, \qquad \hat{\mathcal{F}}_y = \frac{1}{\sqrt{2}}\begin{pmatrix} 0 & -\mathrm{i} & 0 \\ \mathrm{i} & 0 & -\mathrm{i} \\ 0 & \mathrm{i} & 0 \end{pmatrix}, \qquad \hat{\mathcal{F}}_z = \begin{pmatrix} 1 & 0 & 0 \\ 0 & 0 & 0 \\ 0 & 0 & -1 \end{pmatrix} . \tag{2.3}$$

In addition to that, one can define the quadrupole operators as

$$\hat{\mathcal{Q}}_{ij} = \{\hat{\mathcal{F}}_i, \hat{\mathcal{F}}_j\} - \frac{4}{3}\delta_{ij}\hat{\mathcal{N}} , \tag{2.4}$$

where $\{\hat{\mathcal{Q}}_{xz}, \hat{\mathcal{Q}}_{xy}, \hat{\mathcal{Q}}_{zz}, \hat{\mathcal{V}}_x = 1/2(\hat{\mathcal{Q}}_{xx} - \hat{\mathcal{Q}}_{yy}), \hat{\mathcal{V}}_y = \hat{\mathcal{Q}}_{xy}\}$ are the additional generators for the entire spin-1 algebra. $\hat{\mathcal{N}}$ denotes the identity matrix. For their matrix and second quantization representation, see Appendix A.1. A general density operator for the spin-1 system can now be expressed as

$$\hat{\rho} = \frac{1}{3}\hat{\mathcal{N}} + \sum_i f_i \hat{\mathcal{F}}_i + \sum_j q_j \hat{\mathcal{Q}}_{jz} + \sum_k v_k \hat{\mathcal{V}}_k \,. \tag{2.5}$$

Equivalent to the magnetization sphere are the subsets $\{\hat{\mathcal{Q}}_{yz}, \hat{\mathcal{Q}}_{xz}, \hat{\mathcal{F}}_z\}$ and $\{\hat{\mathcal{V}}_x, \hat{\mathcal{V}}_y, \hat{\mathcal{F}}_z\}$. The first two operators are connected through a rotation generated by $\hat{\mathcal{F}}_z$ with the Larmor phase as the parameter. The transversal operators can be defined as

$$\begin{aligned} \hat{\mathcal{F}}_\perp &\equiv \cos\varphi_\mathrm{L} \hat{\mathcal{F}}_x + \sin\varphi_\mathrm{L} \hat{\mathcal{F}}_y \\ \hat{\mathcal{Q}}_\perp &\equiv \cos\varphi_\mathrm{L} \hat{\mathcal{Q}}_{yz} - \sin\varphi_\mathrm{L} \hat{\mathcal{Q}}_{xz} \\ \hat{\mathcal{V}}_\perp &\equiv \cos 2\varphi_\mathrm{L} \hat{\mathcal{V}}_x + \sin 2\varphi_\mathrm{L} \hat{\mathcal{V}}_y \,. \end{aligned} \tag{2.6}$$

In the ongoing project, magnetic domain walls in the easy-plane phase (see Section 2.6.2) are of interest, where the ground state is a spin in the $\hat{\mathcal{F}}_x$-$\hat{\mathcal{F}}_y$ plane, so $\hat{\mathcal{F}}_\perp$ is the relevant operator. Nonetheless, the three subspaces are connected through the spinor phase, which is further described in Section 2.2. This is of particular interest for describing a specific property of the Bose-Einstein condensate (BEC), because φ_S represents the right parameter for a special domain wall [37], the so-called sine-Gordon (sG) soliton discussed in Section 2.7.

2.2 Spin-nematic sphere

As mentioned above, $\hat{\mathcal{F}}_\perp$ and $\hat{\mathcal{Q}}_\perp$ are connected by a rotation around $\hat{\mathcal{Q}}_{zz}$, parametrized through the spinor phase φ_S. Since this connection is relevant for the experiment, one can define a more practical operator

$$\hat{\mathcal{Q}}_0 \equiv -\frac{1}{3}\hat{\mathcal{N}} - \hat{\mathcal{Q}}_{zz} \,. \tag{2.7}$$

The unitary rotation is the same except for the orientation, but the spectrum is centered around zero. The subspace $\{\hat{\mathcal{F}}_\perp(\varphi_\mathrm{L}), \hat{\mathcal{Q}}_\perp(\varphi_\mathrm{L}), \hat{\mathcal{Q}}_0(\varphi_\mathrm{L})\}$ is called the spin-nematic sphere for each phase φ_L [13]. While the commutators obey the relation $[\hat{\mathcal{Q}}_0, \hat{\mathcal{Q}}_\perp(\varphi_\mathrm{L})] = 2\mathrm{i}\hat{\mathcal{F}}_\perp(\varphi_\mathrm{L})$ and $[\hat{\mathcal{F}}_\perp(\varphi_\mathrm{L}), \hat{\mathcal{Q}}_0] = 2\mathrm{i}\hat{\mathcal{Q}}_\perp(\varphi_\mathrm{L})$, it is important to notice that the commutator of $\hat{\mathcal{Q}}_\perp$ and $\hat{\mathcal{F}}_\perp$ is dependent on φ_L

$$[\hat{\mathcal{Q}}_\perp(\varphi_\mathrm{L}), \hat{\mathcal{F}}_\perp(\varphi_\mathrm{L})] = 2\mathrm{i}\hat{\mathcal{Q}}_0 + \mathrm{i}(\hat{\mathcal{N}}^+ - \hat{\mathcal{V}}_\perp(\varphi_\mathrm{L})) \,; \qquad \hat{\mathcal{N}}^+ \equiv (\mathbb{1}_3 - \hat{\mathcal{Q}}_0)/2 \,. \tag{2.8}$$

So in general, the subset $\{\hat{\mathcal{F}}_\perp(\varphi_\mathrm{L}), \hat{\mathcal{Q}}_\perp(\varphi_\mathrm{L}), \hat{\mathcal{Q}}_0(\varphi_\mathrm{L})\}$ does not fulfill the $\mathfrak{su}(2)$ commutation relation, but one can find a value of φ_L for states with equal population in $|m_\mathrm{F} = \pm 1\rangle$ (this is the measure of the operator $\hat{\mathcal{N}}^+$), where $\langle \hat{\mathcal{N}}^+ - \hat{\mathcal{V}}_\perp(\varphi_\mathrm{L})\rangle$ vanishes. Because none of the three operators generate a change in the Larmor phase, the SU(2) permutation

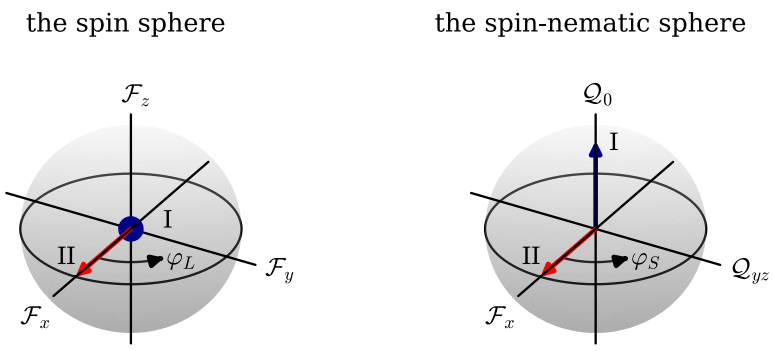

Figure 2.1: Main initial states on the spin sphere and spin-nematic sphere: The polar state (I) with all atoms in the zero component is located on the north pole of the spin-nematic sphere but is not on the surface of the spin sphere, as it has no magnetization. In contrast, the easy plane state (II) with $\varphi_\mathrm{L}\&\varphi_\mathrm{S} = 0 \hat{=} |F_x\rangle$ is visible on both spheres. The rotation generated by $\hat{\mathcal{F}}_z$ is parametrized by the Larmor phase φ_L, while the rotation around $\hat{\mathcal{Q}}_0$ is the spinor phase φ_S.

relation for the expectation value is fulfilled and remains valid during the evolution [21]

$$\langle[\hat{\mathcal{Q}}_\perp(\varphi_\mathrm{L}), \hat{\mathcal{F}}_\perp(\varphi_\mathrm{L})]\rangle = 2\mathrm{i}\langle\hat{\mathcal{Q}}_0\rangle\,. \tag{2.9}$$

Two specific initial states are relevant in this thesis: The polar state $|\Psi_p\rangle$ and the ground state of the easy plane phase with maximal transversal spin length $|\Psi_{EP}\rangle$. The easy-plane (EP) is a specific phase of the many-particle BEC description and will be further discussed in Section 2.6.

These two states are defined as

$$|\Psi_p\rangle = \begin{pmatrix} 0 \\ 1 \\ 0 \end{pmatrix}\,, \qquad |\Psi_{EP}\rangle = \begin{pmatrix} \frac{1}{2}\mathrm{e}^{\mathrm{i}\varphi_\mathrm{L}} \\ \frac{1}{\sqrt{2}}\mathrm{e}^{\mathrm{i}\varphi_\mathrm{S}} \\ \frac{1}{2}\mathrm{e}^{-\mathrm{i}\varphi_\mathrm{L}} \end{pmatrix}\,. \tag{2.10}$$

The expectation value of $\langle\Psi_p|\,\hat{\mathcal{Q}}_0\,|\Psi_p\rangle$ is one, which is represented on the north pole of the spin-nematic sphere, as can be seen in Fig. 2.1, but the expectation value of the magnetization is zero. This state is not on the surface of the spin sphere but in the center. In contrast, $\langle\Psi_{EP}|\,\hat{\mathcal{Q}}_0\,|\Psi_{EP}\rangle = 0$ and for $\varphi_\mathrm{L} = \varphi_\mathrm{S} = 0$, $\langle\hat{\mathcal{F}}_x\rangle = 1$, which corresponds to a maximal transversal spin length $\langle\hat{\mathcal{F}}_\perp\rangle = 1$. This state is represented on both spheres along the $\hat{\mathcal{F}}_x$ axis and the initial condition for the experiment shown in Section 4.5. On the one hand, if the state is rotated around $\hat{\mathcal{F}}_z$ via the Larmor phase of $\varphi_\mathrm{L} = \pi/2$, the state has still maximal transversal spin length, but lies not any more on the spin-nematic sphere. On the other hand, if the state is rotated around $\hat{\mathcal{Q}}_0$ via a change of the spinor phase $\varphi_\mathrm{S} = \pi/2$, the transversal spin length is reduced to zero but the quadrupole moment is maximized with $\langle\hat{\mathcal{Q}}_{yz}\rangle = 1$.

2.3 Multiple atoms in a Bose-Einstein condensate

In an experiment with $N \approx 10^5$ particles, the Hilbert space is not any more three dimensional as the one of a single spin-1 atom but $d = 3^N$. The operators are now acting on a specific atom of the cloud, so they have to be extended to collective operators $\hat{O}_{i,coll} = \sum_{n=1}^{N} \hat{\mathcal{O}}_{i,n}$, where $\hat{\mathcal{O}}_i$ corresponds to the spin-1 operators previously presented. Since ^{87}Rb is bosonic, the dimension reduces to $d = {}^{(N+2)(N+1)}/_{2}$. A state is now described in the Fock basis with $|\Psi\rangle = |N_{+1}, N_0, N_{-1}\rangle$ with the atom number in the respective substate N_{m_F} and one can express now the operators in second quantization using the Jordan-Schwinger map [16, 35]

$$\hat{O}_i = \left(\hat{a}_{+1}^\dagger, \hat{a}_0^\dagger, \hat{a}_{-1}^\dagger\right) \hat{\mathcal{O}}_i \begin{pmatrix} \hat{a}_{+1} \\ \hat{a}_0 \\ \hat{a}_{-1} \end{pmatrix} , \tag{2.11}$$

where $\hat{a}_m^\dagger$ ($\hat{a}_m$) is the creation (annihilation) operator of the respective substate m with the commutation relation $[\hat{a}_m, \hat{a}_n^\dagger] = \delta_{mn}$. A definition of all operators in single particle description and second quantization is given in Appendix A.1. Since the commutation relations remain unchanged, the generalized spin sphere and spin-nematic sphere are spanned by the collective operators equivalent to the single-atom spheres, $\{\hat{F}_x, \hat{F}_y, \hat{F}_z\}$ for the spin sphere and $\{\hat{F}_\perp(\varphi_\mathrm{L}), \hat{Q}_\perp(\varphi_\mathrm{L}), \hat{Q}_0(\varphi_\mathrm{L})\}$ for the spin-nematic sphere. For convenience, the axis are normalized by the the total atom number N to keep a radius of one.

2.4 Projective measurement

In quantum mechanics, a measurement of the observable M projects a state $\hat{\rho}$ to the respective eigenspace via the projectors $\hat{P}_m$ [29]

$$\hat{M} = \sum_m m \hat{P}_m \, . \tag{2.12}$$

m are the eigenvalues and $p(m) = \langle\psi| \hat{P}_m |\psi\rangle$ is the probability of the result m. The operators have to satisfy $\sum_m \hat{M}_m^\dagger \hat{M}_m = 1$ and have to be orthogonal, $\hat{M}_m \hat{M}_n = \delta_{mn} \hat{M}_m$. In the spin-1 case, the magnetic substates can in practice be separated and the respective particle density gained by first applying a magnetic field gradient in Z-direction using the Zeeman effect, then illuminate with resonant light. For the experimental details see Section 3.1.3. One measurement gives in second quantization the operators of the respective sublevels

$$\begin{aligned} \hat{N}_{+1} = \hat{a}_{+1}^\dagger \hat{a}_{+1} &= \frac{1}{3}\hat{N} + \frac{1}{2}\hat{F}_z + \frac{1}{4}\hat{Q}_{zz} \\ \hat{N}_0 = \hat{a}_0^\dagger \hat{a}_0 &= \frac{1}{3}\hat{N} - \frac{1}{2}\hat{Q}_{zz} \\ \hat{N}_{-1} = \hat{a}_{-1}^\dagger \hat{a}_{-1} &= \frac{1}{3}\hat{N} - \frac{1}{2}\hat{F}_z + \frac{1}{4}\hat{Q}_{zz} \, . \end{aligned} \tag{2.13}$$

These can be decomposed and expressed by the previously introduced spin-1 operators. The Fock state can now be reconstructed by the atom number of the respective substates,

which are the experimental expectation values of the operators $N_{m_\mathrm{F}} = \langle \hat{N}_{m_\mathrm{F}} \rangle$. One can further reconstruct the values for the observables F_z and Q_{zz} with a linear combination of the sublevel counts, e.g. $F_z = N^- = N_{+1} - N_{-1}$.

For a d-dimensional Hilbert space, the expectation value of up to $d-1$ operators can be measured. The total atom number takes one dimension, and all other measurement operators must commute. To measure in a different basis, a unitary transformation $\hat{U}$ has to be applied before the measurement, which is changing the measured atom number distribution in the sublevels to $N'_{m_\mathrm{F}} = \langle \hat{U}^\dagger \hat{N}_{m_\mathrm{F}} \hat{U} \rangle$. To measure for example the F_x observable, a $\pi/2$ rotation around $\hat{F}_y$ can be applied: $\hat{U} = \mathrm{e}^{-\mathrm{i}\pi/2 \hat{F}_y}$. As mentioned, all operators have to commute, so to extract a phase difference between two non-commuting observables like $F_x \& F_y$, i.e., the Larmor phase, another method has to be used, which is described in the following Section 2.5.

2.5 Positive Operator-Valued Measure

As mentioned above, in the three dimensional spin-1 system only two observables can be measured in a single realization. To extract also non-commuting operators, the Positive Operator-Valued Measure (POVM) formalism can be used [9, 29, 38]. The difference to a projective measurement is the definition of the POVM elements $\hat{E}_m$ of a measurement operator $\hat{M}_m$ with the outcome m

$$\hat{E}_m \equiv \hat{M}_m^\dagger \hat{M}_m \tag{2.14}$$

The probability of outcome m is $p(m) = \langle \psi | \hat{M}_m^\dagger \hat{M}_m | \psi \rangle = \langle \psi | \hat{E}_m | \psi \rangle$, so $\hat{E}_m$ is a positive operator while still satisfying $\sum_m \hat{E}_m = 1$. If the operators are orthogonal, a POVM and projective measurement are identical, but POVM elements $\hat{E}_m$ do not necessarily have to be orthogonal. It follows, that more measurable elements can be defined than a projective measurement would allow, here an example taken from Kunkel [21]

$$\begin{aligned}
\hat{E}_0 &= \frac{1}{6}\hat{N} + \frac{1}{4}\hat{F}_x + \frac{1}{8}\hat{V}_x - \frac{1}{16}\hat{Q}_{zz}\,, & \hat{E}_1 &= \frac{1}{6}\hat{N} - \frac{1}{4}\hat{V}_x + \frac{1}{8}\hat{Q}_{zz}\,, \\
\hat{E}_2 &= \frac{1}{6}\hat{N} - \frac{1}{4}\hat{F}_x + \frac{1}{8}\hat{V}_x - \frac{1}{16}\hat{Q}_{zz}\,, & & \\
\hat{E}_3 &= \frac{1}{6}\hat{N} + \frac{1}{4}\hat{F}_z + \frac{1}{8}\hat{Q}_{zz}\,, & \hat{E}_4 &= \frac{1}{6}\hat{N} - \frac{1}{4}\hat{Q}_{zz}\,, \\
\hat{E}_5 &= \frac{1}{6}\hat{N} - \frac{1}{4}\hat{F}_z + \frac{1}{8}\hat{Q}_{zz}\,. & &
\end{aligned} \tag{2.15}$$

It is easy to prove that $\sum_m \hat{E}_m = \hat{N}$, which is equal to the identity taking the normalization into account. While the first three elements refer to a measurement of the F_x observable, the second three elements originate from a F_z measurement. As a conclusion, it is possible to extract two non-commuting observables in one single measurement with this formalism.

But there is another problem: in the spin-1 system, there are only three possible elements to measure. This can also be overcome via using the $F = 2$ manifold, which is unoccupied

during all measurements using this readout formalism presented in this thesis. The hyperfine states in $F = 2$ are individually addressable in the microwave range, which gives eight states in total to use. A projective measurement in the enlarged Hilbert space is then performed to read out the desired observables, which is known as Naimark's extension [15]. For this, the populations in the magnetic sub-levels $|F = 1, m_1\rangle$ can be coupled via microwave (MW) pulses to the sublevels of $|F = 2, m_2\rangle$, referred as coupling pulses

$$C_x^{m_1 m_2} = \frac{1}{2} a^\dagger_{1,m_1} a_{2,m_2} + h.c. \tag{2.16}$$

$$C_y^{m_1 m_2} = \frac{\mathrm{i}}{2} a^\dagger_{1,m_1} a_{2,m_2} + h.c. \,. \tag{2.17}$$

Afterwards, a selective radiofrequency (RF) pulse in the $F = 1$ manifold can rotate the system as discussed in Section 2.4. An observable is "stored" in the second level before rotating the first level into another frame. So far, readout schemes for the transverse spin length $\{F_x, F_y\}$ ($F_\perp$ readout), for the full spin sphere $\{F_x, F_y, F_z\}$ and for the spinor phase $\{F_x, Q_{yz}\}$ have been developed and used [21]. In the following Sections 2.5.1 and 2.5.2, this thesis expands the spinor phase readout to the full spin-nematic sphere $\{F_x, Q_{yz}, Q_0\}$, as well as establishes a dual-phase readout (DuPR) with the observables $\{F_x, F_y, Q_{yz}, Q_0\}$.

2.5.1 Full spin-nematic readout

To reconstruct a state on the spin-nematic sphere, the observables $\{F_x, Q_{yz}, Q_0\}$ need to be measured. Q_0 is connected to Q_{zz} via Eq. (2.7), which can be measured without any rotation, as shown previously in Eq. (2.13). The first steps in the sequence are consequently two coupling pulses between $|F = 1, m_\mathrm{F} = \pm 1\rangle$ and $|F = 2, m_\mathrm{F} = \pm 1\rangle$. This is similar to the storage of F_z in the $F_\perp$ readout [22], followed by the sequence of the spinor phase readout presented in [21]. The whole unitary rotation is given as

$$\begin{aligned}\hat{U} =& e^{-\mathrm{i}\pi/2 \hat{F}_y} \cdot e^{-\mathrm{i}\pi C_x^{00}} \cdot e^{-i\pi C_y^{00}} \cdot e^{-i\pi/2 \hat{F}_y} \cdot e^{-i\pi \hat{F}_y} \\ & \cdot e^{-i\pi/2 C_y^{00}} \cdot e^{-i\pi/2 C_y^{12}} \cdot e^{-i\pi/2 C_y^{-1-2}} \cdot e^{-i\pi/2 \hat{F}_y} \cdot e^{-i\varphi C_y^{11}} \cdot e^{-i\varphi C_y^{-1-1}}\end{aligned} \tag{2.18}$$

Not considered here is the time evolution between the pulse steps, which includes spin echo to reduce the noise. The angle φ in the first coupling pulses is chosen to be variable in the calculation, later on $\varphi = \arctan(1/\sqrt{2})$ is used to store $1/3$ of the population for each observable. The calculation for the new POVM elements $\hat{N}'_{F,m_\mathrm{F}} = \hat{U}^\dagger \hat{N}_{F,m_\mathrm{F}} \hat{U}$ are carried out by hand in second quantization, a summary of the individual rotation steps is listed in Appendix A.2. Terms including creation or annihilation operators of the $F = 2$ manifold in linear or second order, namely $\hat{a}_{2,m_2} \& \hat{a}^\dagger_{2,m_2}$, are summarized in the $\hat{f}_i$ operators. These do not contribute to the POVM elements because the $F = 2$ manifold is initially unoccupied.

$$
\begin{aligned}
\hat{N}'_{1,1} &= \frac{1}{4}\hat{N}_0 + \frac{\cos^2(\varphi/2)}{8}\left(\hat{V}_x + \hat{N}_+\right) + \frac{\cos(\varphi/2)}{4}\hat{Q}_{yz} + \hat{f}_1 \\
\hat{N}'_{1,0} &= \cos^2(\varphi/2)\left(\frac{1}{6}\hat{N} + \frac{1}{8}\hat{Q}_{zz} - \frac{1}{4}\hat{V}_x\right) + \hat{f}_2 \\
\hat{N}'_{1,-1} &= \frac{1}{4}\hat{N}_0 + \frac{\cos^2(\varphi/2)}{8}\left(\hat{V}_x + \hat{N}_+\right) - \frac{\cos(\varphi/2)}{4}\hat{Q}_{yz} + \hat{f}_3 \\
\hat{N}'_{2,2} &= \frac{1}{4}\hat{N}_0 + \frac{\cos^2(\varphi/2)}{8}\left(\hat{V}_x + \hat{N}_+\right) - \frac{\cos(\varphi/2)}{4}\hat{F}_x + \hat{f}_4 \\
\hat{N}'_{2,1} &= \sin^2(\varphi/2)\left(\frac{1}{3}\hat{N} + \frac{1}{4}\hat{Q}_{zz} + \frac{1}{2}\hat{F}_z\right) + \hat{f}_5 \\
\hat{N}'_{2,0} &= \cos^2(\varphi/2)\left(\frac{1}{3}\hat{N} + \frac{1}{4}\hat{Q}_{zz} - \frac{1}{2}\hat{V}_x\right) + \hat{f}_6 \\
\hat{N}'_{2,-1} &= \sin^2(\varphi/2)\left(\frac{1}{3}\hat{N} + \frac{1}{4}\hat{Q}_{zz} - \frac{1}{2}\hat{F}_z\right) + \hat{f}_7 \\
\hat{N}'_{2,-2} &= \frac{1}{4}\hat{N}_0 + \frac{\cos^2(\varphi/2)}{8}\left(\hat{V}_x + \hat{N}_+\right) + \frac{\cos(\varphi/2)}{4}\hat{F}_x + \hat{f}_8\,.
\end{aligned}
\tag{2.19}
$$

Taking linear combinations, one gets the desired observable set including F_z, as it is included in the non-rotated measurement. The final observables can be calculated now in an experiment through Eq. (2.20) and further be normalized by the total atom number N. In Section 4.3 will be shown a measurement for the verification of this readout. The theoretical detail of this experiment is discussed in Section 2.6.1.

$$
\begin{aligned}
F_x &= \frac{2}{\cos(\varphi/2)}\left(N'_{2,-2} - N'_{2,2}\right) \\
Q_{yz} &= \frac{2}{\cos(\varphi/2)}\left(N'_{1,1} - N'_{1,-1}\right) \\
Q_0 &= N - \frac{2}{\sin^2(\varphi/2)}\left(N'_{2,1} + N'_{2,-1}\right) \\
F_z &= \frac{1}{\sin^2(\varphi/2)}\left(N'_{2,1} - N'_{2,-1}\right)\,.
\end{aligned}
\tag{2.20}
$$

2.5.2 Dual-phase readout

To this point, it was possible to extract the transverse spin length $F_\perp$ and the spinor phase φ_S in two separate measurements. But it was necessary in the recent project to measure both observables simultaneously. Following the POVM formalism, a readout sequence is developed and calculated that allows to extract up to four non-commuting observables in a single measurement. The dual-phase readout (DuPR) includes $\{F_x, F_y, Q_{yz}, Q_0\}$ and

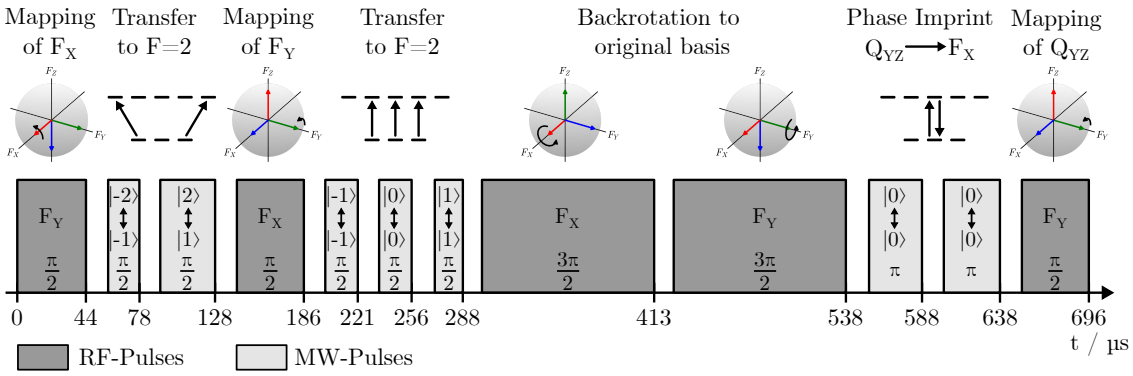

Figure 2.2: Dual-phase readout sequence: Following the POVM formalism [22], the system is first rotated around the $\hat{F}_y$ axis, to further store $1/3$ of the population from $|F=1, m_\mathrm{F}=\pm1\rangle$ in the F=2 manifold $|F=2, m_\mathrm{F}=\pm2\rangle$. This will store the F_x observable for the imaging. Then, after a rotation around $\hat{F}_x$ in the $F=1$ components, the F_y observable is stored the same way in $|F=2, m_\mathrm{F}=\pm1\rangle$. In addition to that, Q_0 can later be extracted via the difference in population of $|F=1, m_\mathrm{F}=0\rangle$ and $|F=2, m_\mathrm{F}=0\rangle$. Two RF pulses rotate the system to the starting orientation, before two π coupling pulses map Q_{yz} to F_x. This can now be extracted in the F=1 manifold after another $\hat{F}_y$ rotation.

the unitary rotation U is in this case:

$$\begin{aligned} U =& \mathrm{e}^{-\mathrm{i}\pi/2\hat{F}_y} \cdot \mathrm{e}^{-\mathrm{i}\pi C_x^{00}} \cdot \mathrm{e}^{-\mathrm{i}\pi C_y^{00}} \cdot \mathrm{e}^{-\mathrm{i}3\pi/2\hat{F}_y} \cdot \mathrm{e}^{-\mathrm{i}3\pi/2\hat{F}_x} \\ & \cdot \mathrm{e}^{-\mathrm{i}\pi/2 C_y^{00}} \mathrm{e}^{-\mathrm{i}\pi/2 C_y^{11}} \cdot \mathrm{e}^{-\mathrm{i}\pi/2 C_y^{-1-1}} \\ & \cdot \mathrm{e}^{-\mathrm{i}\pi/2\hat{F}_x} \cdot \mathrm{e}^{-\mathrm{i}\varphi C_y^{12}} \cdot \mathrm{e}^{-\mathrm{i}\varphi C_y^{-1-2}} \cdot \mathrm{e}^{-\mathrm{i}\pi/2\hat{F}_y} \,. \end{aligned} \tag{2.21}$$

The complete time sequence is visualized in Fig. 2.2. The system is first rotated around the $\hat{F}_y$ axis and φ chosen so that $1/3$ of the population is stored from $|F=1, m_\mathrm{F}=\pm1\rangle$ in the $F=2$ manifold, $|F=2, m_\mathrm{F}=\pm2\rangle$. Then, after a rotation around $\hat{F}_x$, one half of the remaining population in $|F=1, m_\mathrm{F}=\pm1\rangle$ is stored together with $|F=1, m_\mathrm{F}=0\rangle$ in $|F=2, m_\mathrm{F}=0, \pm1\rangle$. The coupling between $|F=1 \leftrightarrow 2, 0\rangle$ is not necessary for the purpose of reading out both phases, but it does offer the possibility of including Q_0 in the observation variables. Two $3\pi/2$ RF pulses rotate the system back to the starting orientation, before two π coupling pulses advance the phase between φ_0 and $\varphi_{\pm1}$, namely advance the spinor phase and map $\hat{Q}_{yz}$ to $\hat{F}_x$. After another rotation around $\hat{F}_y$, Q_{yz} is

now measurable in the $F = 1$ manifold. The new populations read:

$$
\begin{aligned}
N'_{11} &= \cos^2\frac{\phi}{2}\left(\frac{1}{6}N - \frac{1}{16}Q_{zz} + \frac{1}{8}V_x + \frac{1}{4}Q_{yz}\right)\\
N'_{10} &= \frac{1}{6}N + \frac{1}{8}Q_{zz} - \frac{1}{4}V_x\\
N'_{1-1} &= \cos^2\frac{\phi}{2}\left(\frac{1}{6}N - \frac{1}{16}Q_{zz} + \frac{1}{8}V_x - \frac{1}{4}Q_{yz}\right)\\
N'_{22} &= \sin^2\frac{\phi}{2}\left(\frac{1}{3}N - \frac{1}{8}Q_{zz} + \frac{1}{4}V_x - \frac{1}{2}F_x\right)\\
N'_{21} &= \frac{1}{4}\cos^2\frac{\phi}{2}N_{10} + \frac{1}{12}N + \frac{1}{16}Q_{zz} - \frac{1}{8}V_x + \frac{1}{4}\cos\frac{\phi}{2}F_y\\
N'_{20} &= \cos^2\frac{\phi}{2}\left(\frac{1}{6}N + \frac{1}{8}Q_{zz} + \frac{1}{4}V_x\right)\\
N'_{2-1} &= \frac{1}{4}\cos^2\frac{\phi}{2}N_{10} + \frac{1}{12}N + \frac{1}{16}Q_{zz} - \frac{1}{8}V_x - \frac{1}{4}\cos\frac{\phi}{2}F_y\\
N'_{2-2} &= \sin^2\frac{\phi}{2}\left(\frac{1}{3}N - \frac{1}{8}Q_{zz} + \frac{1}{4}V_x + \frac{1}{2}F_x\right)\ .
\end{aligned}
\tag{2.22}
$$

With this, the desired operators can be calculated as before via linear combination of the POVM elements in Eq. (2.26). The outcome of this readout is compared with the existing readouts in the experiments on the sG solitons, which will be described in Section 2.7.

$$F_x = \frac{1}{\sin^2\phi/2}\left(N'_{2-2} - N'_{22}\right) \tag{2.23}$$

$$F_y = \frac{2}{\cos\phi/2}\left(N'_{21} - N'_{2-1}\right) \tag{2.24}$$

$$Q_{yz} = \frac{2}{\cos^2\phi/2}\left(N'_{11} - N'_{1-1}\right) \tag{2.25}$$

$$Q_0 = N - 4\left(\frac{N'_{20}}{\cos^2\phi/2} + N'_{10}\right)\ . \tag{2.26}$$

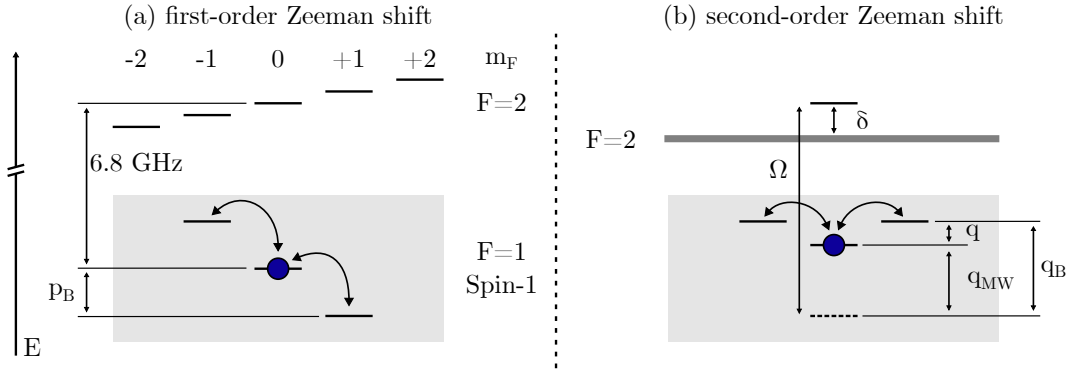

Figure 2.3: First and second order Zeeman shifts in the rubidium system: (a) The first-order Zeeman shift has the energy difference $p_B \approx 700$ kHz/G, but is not the relevant energy scale in the description of spin-changing collisions (SCC). (b) The effective second-order Zeeman shift $q = q_B - q_{MW}$ is controlled by far-detuned MW dressing with detuning δ, which reduces $q_B \approx 72$ Hz/G^2 for precise control of the interaction strength. Adapted from [31]

2.6 Energy landscape

The Hamiltonian of the system can be split into three parts, the single particle Hamiltonian $\hat{H}_{sp}$, the magnetic Hamiltonian $\hat{H}_B$ and the interaction potential $\hat{V}_{int}$. The single particle Hamiltonian is hereby given as $\hat{H}_{sp} = -\frac{\hbar}{2M}\nabla^2 + V_{trap}$ and the bosonic many-body Hamiltonian with pairwise interactions $\hat{H}_{int}$ reads [34]

$$\hat{H} = \sum_{ij} \hat{H}^{sp}_{ij} \hat{a}^\dagger_i \hat{a}_j + \frac{1}{2} \sum_{ijkm} \langle ij|\hat{V}_{int}|km\rangle \hat{a}^\dagger_i \hat{a}^\dagger_j \hat{a}_k \hat{a}_m \tag{2.27}$$
$$\hat{H}^{sp}_{ij} = \int \mathrm{d}^3x \; \tilde{\mathbf{\Phi}}^*_i(\mathbf{x}) \hat{H}_{sp} \tilde{\mathbf{\Phi}}_j(\mathbf{x}) \, .$$

$\hat{a}^\dagger_i$ ($\hat{a}_i$) are the bosonic creation (annihilation) operators and $\tilde{\mathbf{\Phi}}_i(\mathbf{x})$ the basis state wavefunctions. While $\tilde{\mathbf{\Phi}}_0(\mathbf{x})$ describes the BEC, the remaining ones are for the completeness. One can further write this in bosonic field operators $\hat{\mathbf{\Psi}}(\mathbf{x}) = \sum_i \hat{a}_i \tilde{\mathbf{\Phi}}_i(\mathbf{x})$ with the same commutation relations. The many-body Hamiltonian therefore reads

$$\hat{H} = \int \mathrm{d}^3x \; \hat{\mathbf{\Psi}}^\dagger(\mathbf{x}) H^{sp} \hat{\mathbf{\Psi}}(\mathbf{x}) + \frac{1}{2} \int \mathrm{d}^3x \; \hat{\mathbf{\Psi}}^\dagger(\mathbf{x}) \hat{\mathbf{\Psi}}^\dagger(\mathbf{x}') V_{int}(\mathbf{x} - \mathbf{x}') \hat{\mathbf{\Psi}}(\mathbf{x}') \hat{\mathbf{\Psi}}(\mathbf{x}) \tag{2.28}$$

While dealing with $\sim 10^5$ atoms, it is not practical to describe each atom individually. One property of a BEC is, that all atoms are occupying the same ground state. It is thus convenient and sufficient to describe the dynamics on a mean-field level, where quantum fluctuations and entanglement are neglected. The field operators can thus be replaced by

complex-valued functions $\psi(\mathbf{x},t)$ [18]

$$\psi(\mathbf{x},t) = \langle\hat{\mathbf{\Psi}}(\mathbf{x},t)\rangle = \begin{pmatrix} \sqrt{n_{+1}(\mathbf{x},t)}\mathrm{e}^{+\mathrm{i}\varphi_\mathrm{L}(\mathbf{x},t)} \\ \sqrt{n_{+0}(\mathbf{x},t)}\mathrm{e}^{\mathrm{i}\varphi_\mathrm{S}(\mathbf{x},t)} \\ \sqrt{n_{-1}(\mathbf{x},t)}\mathrm{e}^{-\mathrm{i}\varphi_\mathrm{L}(\mathbf{x},t)} \end{pmatrix} \tag{2.29}$$

The calculation of the time evolution using Eq. (2.28) leads then to the equation of motion, also called Gross-Pitaevskii equation (GPE) [6]

$$\mathrm{i}\hbar\partial_t\psi(\mathbf{x},t) = \left[-\frac{\hbar^2}{2M}\nabla^2 + V_{trap}(\mathbf{x}) + g|\psi(\mathbf{x},t)|^2\right]\psi(\mathbf{x},t)\,, \tag{2.30}$$

where $\hbar$ is the reduced Planck constant and $g = \int V_{int}^{eff}(\mathbf{x})\mathrm{d}^3x$. Considering for ultracold atoms only two-particle collisions and s-wave scattering, the interaction potential reduces to $g = {}^{4\pi\hbar^2 a}/_M$ with the scattering length a.

All experiments described here are additionally performed in an homogeneous magnetic bias field in Z-direction, the same as the quantization axis. This changes the energies of all magnetic sublevels in the $F = 1$ & $F = 2$ manifold due to the Zeeman effect via

$$E_B/h = g_{1,F}m_\mathrm{F}B_Z + g_{2,F}(4 - m_\mathrm{F})B_Z^2\,. \tag{2.31}$$

$p_B = g_{1,1}B_Z$ is hereby the linear and $q_B = -g_{2,1}B_Z^2$ the second order Zeeman shift, also depicted in Fig. 2.3. The first and second order g-factors $g_{1/2,F}$ are in our system given as [41]

$$g_{1,F} \approx \begin{cases} -702\text{ kHz/G} & \text{for F=1} \\ 700\text{ kHz/G} & \text{for F=2} \end{cases} \qquad g_{2,F} \approx \begin{cases} -72\text{ Hz/G}^2 & \text{for F=1} \\ 72\text{ Hz/G}^2 & \text{for F=2} \end{cases} \tag{2.32}$$

The energy shift can also be expressed in second quantization, where the additional magnetic Hamiltonian reads [21]

$$\hat{H}_B/h = p_B\hat{F}_z - \frac{q_B}{2}\hat{Q}_0\,. \tag{2.33}$$

Since the difference in the $m_\mathrm{F} = \pm1$ gives the magnetization in Z-direction, the first order Zeeman shift translates to an expectation value for F_z, while the difference in the population of $m_\mathrm{F} = \pm1 \leftrightarrow m_\mathrm{F} = 0$ is the origin of an expectation value in Q_0. This value would be fixed for one magnetic field, but as depicted in Fig. 2.3, the second-order Zeeman shift is tuneable via off-resonant MW dressing q_{MW} of the zero level to the $F = 2$ manifold. A large detuning δ prevents the condensate to populate the upper states, but allows precise control of the effective shift $q = q_B - q_{MW}$ between the sublevels.

A closer look at the interaction potential shows that it consists of two parts: the density-density interaction $\hat{V}_d$ and the spin-spin interaction $\hat{V}_{spin}$. These are defined via [39]

$$\hat{V}_{int} = \hat{V}_d + \hat{V}_{spin} = \int \mathrm{d}^3x\left(\frac{c_0}{2} : \hat{n}^2 : + \frac{c_1}{2} : \hat{\mathbf{F}}^2 :\right)\,, \tag{2.34}$$

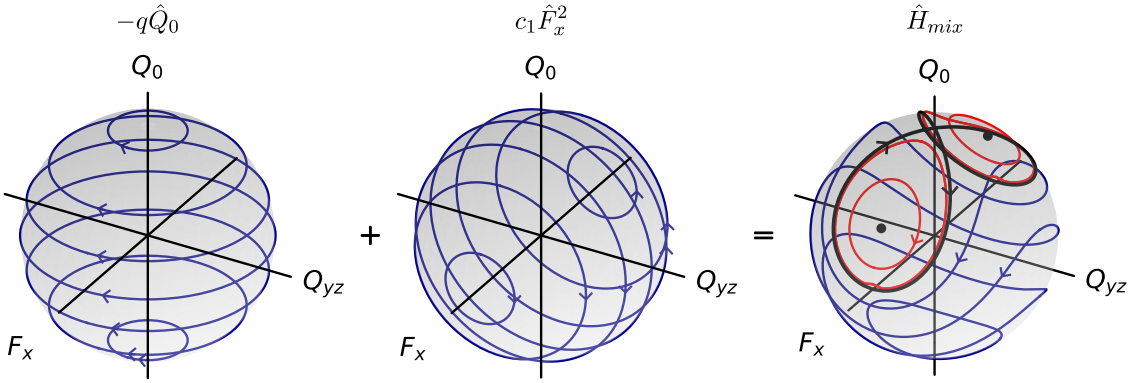

Figure 2.4: Two interaction parts contribute to the spin-mixing process in Eq. (2.36). The first one is a rotation around Q_0, the second one is a shearing around F_x, resulting in combined trajectories. The red ones are trapped rotations around the black dotted fixpoints, the blue curves are a disturbed rotation around the sphere. In between lays the "separatrix", which separates the trapped from the running phase modes. Starting initially in the polar state, the state follows the separatrix during the time evolution. Adapted from [22].

with :: normal ordering, $c_0 = 4\pi\hbar^2(a_0+2a_2)/(3M)$ and $c_1 = 4\pi\hbar^2(a_2-a_0)/(3M)$. $a_{0,2}$ are the scattering lengths between two $F = 1$ atoms for a total angular momentum $F = \{0, 2\}$. Since $c_1 < 0$ in ^{87}Rb, the interaction is ferromagnetic where all spins align to minimize the energy. In this system is also $|c_0| \approx 200|c_1|$ [18], therefore is the dynamic of the density on a smaller scale ξ_d then the dynamic of the spin-spin interaction ξ_s. The spin healing length is defined as $\xi_s = \hbar/k_{xi_s} = \hbar/\sqrt{2Mnc_1}$ and provides the main length scale for the experiments reported here.

2.6.1 Spin-mixing

$\hat{H}_{spin}$ can be rewritten in second quantization in terms of the ladder operators [21]

$$\begin{aligned}\hat{H}_{spin}/h &= \frac{c_1}{2} : \left(\hat{F}_x\hat{F}_x + \hat{F}_y\hat{F}_y + \hat{F}_z\hat{F}_z\right) : \\ &= c_1\hat{N} + c_1\left(\hat{N}_0 - \frac{1}{2}\right)\left(\hat{N}_{+1} + \hat{N}_{-1}\right) + \frac{c_1}{2} : \left(\hat{N}_{+1} - \hat{N}_{-1}\right)^2 : \\ &\quad c_1\left(\hat{a}_0^\dagger\hat{a}_0^\dagger\hat{a}_{+1}\hat{a}_{-1} + \hat{a}_{+1}^\dagger\hat{a}_{-1}^\dagger\hat{a}_0\hat{a}_0\right) . \end{aligned} \tag{2.35}$$

Here, the first three parts are a total energy shift and two relative shifts between the side modes. Because the magnetization is conserved in the experiment, these are not relevant for the description, but the last line represents the spin-mixing process. Together with the second-order Zeeman shift, which is tuneable, the interaction of the spin-mixing is described in

$$\hat{H}_{mix}/h = -\frac{q}{2}\hat{Q}_0 + \frac{c_1}{2}\hat{F}_x^2 . \tag{2.36}$$

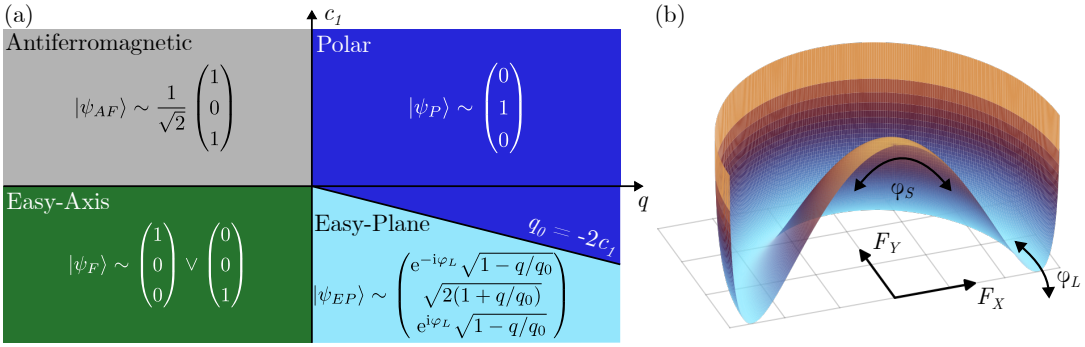

Figure 2.5: (a) Phase diagram of the mean-field ground states in dependence of c_1 and q. c_1 is negative for the ferromagnetic Rubidium-87, but via changing q are three different phases accessible: the in Z-direction magnetized Easy-Axis, the zero magnetized Polar state and the EP phase. (b) Potential landscape of the EP phase: the spin favors maximal length perpendicular to the external magnetic field and can rotate freely around varying the Larmor phase φ_L, but has to climb through a maximum, if the spinor phase φ_S is changed on the spin-nematic sphere.

This process is depicted in Fig. 2.3 with the arrows, where it is also visualized that the first-order Zeeman shift conserves the total energy, but the interaction in the second-order Zeeman shift can be tuned via the dressing q. The dynamic conserves therefore the magnetization as well as the Larmor phase, so the state is represented on the surface of the spin-nematic sphere.

If the state on the north pole of the spin-nematic sphere is prepared (the polar state in Eq. (2.10)), the spin-mixing process causes the system to follow the so-called separatrix, shown in Fig. 2.4. The interaction is quenched from the polar phase to the easy-plane phase described in Section 2.6.2, so this experiment is named "polar quench" and used for the verification of the full-nematic readout in Section 2.5.1, since it only drives dynamic in the spinor phase and Q0.

2.6.2 Mean-field ground state

The physics can now be described in the GPE as

$$\mathrm{i}\hbar\partial_t \mathbf{\Psi}(x,t) = \left[-\frac{\hbar}{2M}\nabla^2 + V_{trap}(\mathbf{x}) + qF_z^2 + \frac{c_0}{2}n(\mathbf{x},t) + \frac{c_1}{2}|\mathbf{F}(\mathbf{x},t)|^2\right]\mathbf{\Psi}(x,t) \qquad (2.37)$$

On can further apply considerations as already mentioned: since the Hamiltonian conserves F_z, the first-order or linear Zeeman splitting can be neglected ($p = 0$). Also the density is in the experiments reported here stationary, so V_{trap} and $c_0 n$ only contribute with a constant offset. Using the remaining parts, the system can be categorized in multiple ground state phases depending on c_1 and q, as shown in Fig. 2.5 (a). Because c_1 being negative, ^{87}Rb is ferromagnetic, so the antiferromagnetic phase is not accessible. But one can reach three phases via changing q: in the easy-axis with negative dressing is the magnetization in the Z-direction favored, as the energy is minimized by occupation of

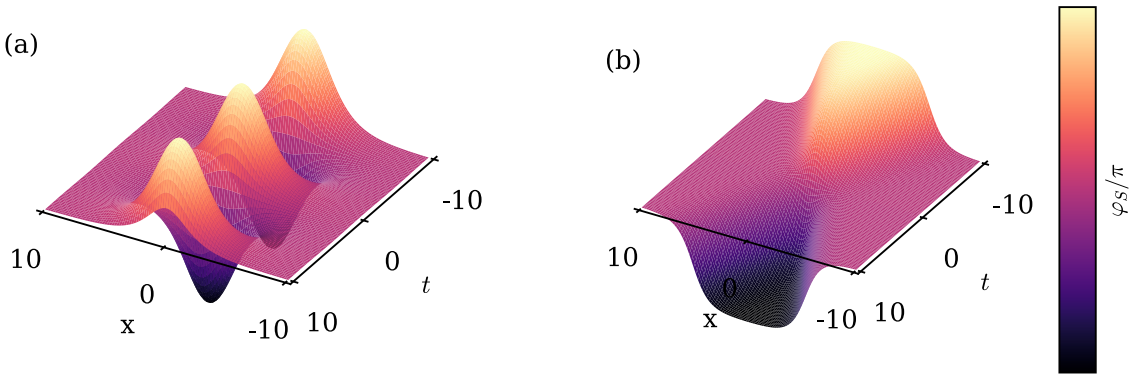

Figure 2.6: Analytical form of (a) a breather from Eq. (2.41) and (b) of a collision between a kink K ($\sigma = +1$) and an anti-kink $\bar{K}$ ($\sigma = -1$) in Eq. (2.40). They restore their shape after passing through each other, resulting in a phase flip compared to the background.

either $m_\mathrm{F} = +1$ or $m_\mathrm{F} = -1$. Tuning q to maximal positive values, $m_\mathrm{F} = 0$ is the ground state with zero magnetization, which is called the Polar state introduced in Section 2.2. The phase in between is the easy-plane (EP), where the ground state has the maximal spin length transversal to the magnetic field for $q \searrow 0$. The potential in the EP takes the form of a "Mexican hat", as shown in Fig. 2.5 (b) for $q = -nc_1 = 1$ [23]:

$$V_{EP} = \frac{nc_1}{2}\left(F_x^2 + F_y^2\right) + \frac{q}{2}\left(1 - \sqrt{1 - \left(F_x^2 + F_y^2\right)}\right) . \tag{2.38}$$

There, the spin can rotate freely in the Larmor phase φ_L. Via changing the spinor phase φ_S on the spin-nematic sphere, only the F_x component reduces the length while F_y remains zero. In Fig. 2.5 (b) is this equivalent to following the potential along the cut on the x-axis.

2.7 Sine-Gordon model

The sine-Gordon (sG) equation is similar to the Klein-Gordon (KG) equation a one-dimensional mathematical model of a real scalar wave field. In contrast to the linear KG model, the sG equation is a non-linear extend and can be approximated around zero to the KG equation. In one spatial dimension, the sG equation reads [5]:

$$\partial_t^2\varphi - \partial_x^2\varphi + \sin\varphi = 0 . \tag{2.39}$$

This equation has two main solutions, which are relativistically invariant:

$$\text{Soliton:} \qquad \varphi(x,t) = 4\arctan\left(\exp\left(\sigma\frac{x-\beta t-x_0}{\sqrt{1-\beta^2}}\right)\right) \tag{2.40}$$

$$\text{Breather:} \qquad \varphi(x,t) = 4\arctan\left((\tan\mu)\frac{\sin(\chi\cos\mu)}{\cosh(Z\sin\mu)}\right) \tag{2.41}$$

$$\chi \equiv \frac{t-\beta/x}{\sqrt{1-\beta^2}} + \chi_0\,, \quad Z \equiv \frac{x-\beta t-x_0}{\sqrt{1-\beta^2}}$$

$\sigma = \pm 1$ is the topological charge for a kink (anti-kink) soliton, $-1 < \beta < 1$ the velocity normed to the speed of light $\beta = {}^{v}/_{c}$ of the solution and $x_0 \& \chi_0$ are arbitrary shifts. $0 < \mu < {}^{\pi}/_{2}$ is the amplitude of the breather [5]. A breather is visualized in Fig. 2.6 (a). The interesting is, that - in the low-energy limit of the transversal ground state - the GPE of the spin-1 system can be approximated by a sG theory in the spinorphase [37]. This simplifies the system to a one-dimensional scalar field theory. However, the low-energy effective field theory (LEEFT) for a pure sG connection is only strictly valid for $q = 0$, otherwise Eq. (2.39) is extended to a double sine-Gordon (DSG) model [37]

$$0 = \partial_t^2\varphi - c_s^2\partial_x^2\varphi - m^2\sin(\varphi) - \frac{\bar{q}}{4}\sin(2\varphi)\,. \tag{2.42}$$

$c_s = \sqrt{2(1-\bar{q}^2)}$ is the free speed of sound and $m = \sqrt{4(1-2\bar{q}^2)}$ is the mass of the sG model. Nevertheless, the unit-less $\bar{q} \equiv {}^{q}/_{2nc_1} \ll 1$ is small, so the DSG addition is only small compared to the dominant sG part for the soliton experiments reported here.

The sG soliton is in our spin-1 system embedded in the spinor phase φ_S as mentioned before. In Fig. 2.7 is the soliton visualized within the spin-1 observables. The soliton profile in red translates in a rotation around the spin-nematic plane, spanned by F_x and Q_{yz}. With an initial system preparation fully in F_x, the soliton builds a domain wall in the transverse spin length $|F_\perp|$. In the sG model is the periodicity 4π, but in the experiment it is half. For the translation of the sG model to the phase in the experiment, one can introduce a factor g, also referred to the interaction strength, with $g = 2$ in the experimental system [20]:

$$0 = \partial_t^2\varphi - c_s^2\partial_x^2\varphi + \frac{m^2}{g}\sin g\varphi \tag{2.43}$$

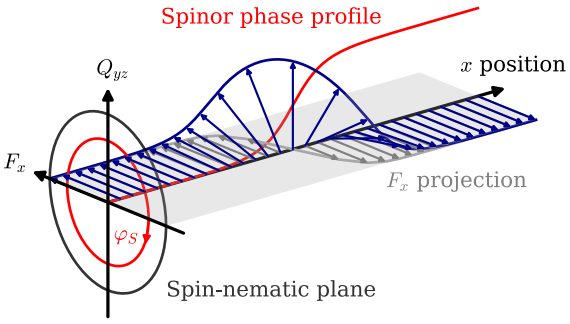

Figure 2.7: The rotation of the spinor phase φ_S around the spin-nematic plane spanned by F_x and Q_{yz} follows the sG soliton profile, depicted in red. This leads to a domain wall in the transversal spin, here exemplary the F_x projection.

This affects also the amplitude and the mass of the sG kink [20], where $m = 2$ and $c_s = \sqrt{2}$

for $q = 0$:

$$\varphi_K(x,t) = \frac{4}{g} \arctan\left(\exp\left(mc_s \frac{x - vt - x_0}{\sqrt{1-(v/c_s)^2}}\right)\right). \tag{2.44}$$

The breather transforms accordingly. An interesting phenomenon is the collision of a kink K and anti-kink $\bar{K}$. In the pure sG theory, they are elastic with the incoming velocity equal to their outgoing velocity. But they interact attractively in the collision region, resulting in a positional shift ahead in their respective propagation direction [5, 20]

$$\delta x = c_s \frac{\sqrt{1-(v/c_s)^2}}{m} \ln\left(\frac{1}{(v/c_s)^2}\right). \tag{2.45}$$

Afterwards, the solitons restore their shape, as depicted in Fig. 2.6 (b). Compared to the background, this results in a phase flip.

3 Rubidium BEC

In this chapter, the experimental platform for the Bose-Einstein condensate (BEC) is presented. It starts with the initial properties of the BEC and continues with the experimental preparation of the initial states. Also the details on the imaging and the measurement of the magnetic field stability are covered. Finally, the setup for the local microwave control is introduced.

3.1 Experimental system

Approximately 10^5 Rubidium-87 atoms are prepared in a quasi-one-dimensional Bose-Einstein condensate (BEC) in a box-like homogeneous trapping potential. This is realized by using a red-detuned elongated laser beam with a wavelength of 1030 nm as a waveguide (WG), resulting in a quasi-one-dimensional harmonic trap with trap frequencies of ($w_r = 2\pi \cdot 170$ Hz and $w_l = 2\pi \cdot 1.6$ Hz [24]). Additional, two blue-detuned laser beams with the wavelength of 760 nm are focused perpendicular to the WG through the imaging objective in reverse direction, see [24] for details. This results in a box-like potential, where the atoms are expanded from the crossed dipole trap (XDT) after condensation. Reducing the intensity of the WG allows control of the final atom number.

All experiments are performed in an external homogeneous magnetic offset field of $B \approx 0.894$ G, which gives rise to the second-order Zeeman shift of $q_B \sim 58$ Hz discussed in Section 2.6. By applying a far off-resonant microwave (MW) dressing, the $|F = 1, m_\mathrm{F} = 0\rangle$ and $|F = 2, m_\mathrm{F} = 0\rangle$ levels are coupled in leading order. This allows to effectively tune q into a regime on the order of the spin interaction.

3.1.1 Preparation of the initial states

The initial condition for all experiments reported here is the (normalized) polar state $\psi_p = \big(0, 1, 0\big)^T$. To get there, all atoms in the beginning are in the state $|F = 1, m_\mathrm{F} = -1\rangle$ after the magnetic trap and condensation. Two consecutive π MW coupling pulses are used between $|1, -1\rangle \leftrightarrow |2, 0\rangle$ and $|2, 0\rangle \leftrightarrow |1, 0\rangle$ to transfer all atoms to the polar state. Remaining atoms in the $|1, \pm 1\rangle$ states are removed via a Stern-Gerlach pulse, i.e., a strong magnetic field gradient pulse. After a settling time of 100 μs for the magnetic field stabilization, the experiment can be continued. Here it is worth to mention that the Larmor phase is initially undefined, since there is no population in $|1, \pm 1\rangle$. The first radiofrequency (RF) rotation sets then the reference. Further, the preparation of the easy plane ground state of $q = 0$ mentioned in Eq. (2.10) is achieved by a $\pi/2$ RF rotation, where the populations occupy $\psi = \left(\frac{1}{2}, \frac{1}{\sqrt{2}}, \frac{1}{2}\right)^T$. To fully elongate the spin along the F_x-axis, the spinor phase also has to be adjusted to $\varphi_\mathrm{S} = (0 \mod 2\pi)$. This is done by the phase difference of two MW π pulses between $|F = 1, m_\mathrm{F} = 0\rangle$ and $|F = 2, m_\mathrm{F} = 0\rangle$.

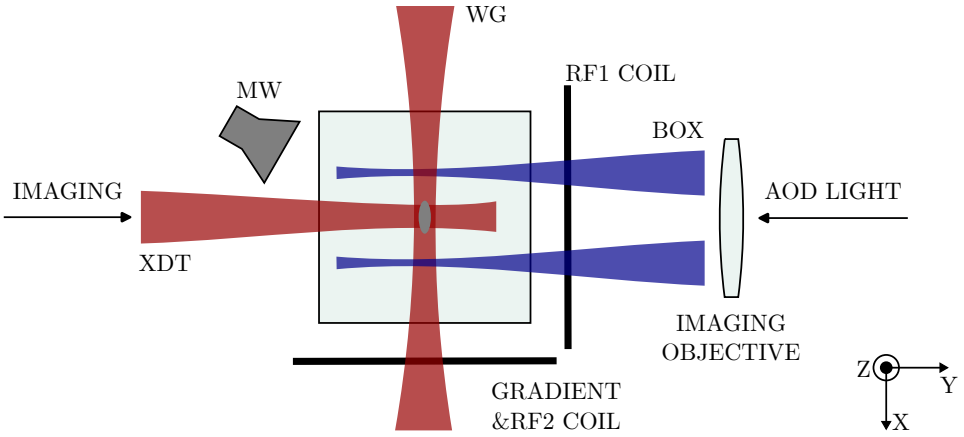

Figure 3.1: Schematic of the experimental setup at the condensate. The BEC is loaded and located at the center of the red-detuned (1030 nm) XDT and WG. Two blue-detuned (760 nm) beams provide repulsive box walls, resulting in a homogeneous 1D condensate. The RF coils and MW antenna are used for the manipulation between the hyperfine states. Adapted from [23]

3.1.2 Experimental generation of sine-Gordon solitons

The ongoing project focuses on the dynamics of sG solitons. The start is a homogeneously elongated transverse spin in the F_x direction, before the phase difference between the $m_F = 0$ and $m_F = \pm 1$ components is locally manipulated to prepare the soliton in the spinor phase. A scheme of the whole procedure is shown in Fig. 3.2. This is done via sequential illumination of the BEC with a steerable laser beam at the tune-out wavelength of 790.032 nm, which induces an additional local magnetic field $\Delta B(x)$ via the vector Stark shift but does not cause density excitations [32]. Illumination in the prepared ground state would now advance the Larmor phase φ_L as a phase difference between the $m_\mathrm{F} = \pm 1$ components, but rubidium-87 has the property that the g factors for the electronic ground states are related via $g_{F=1} \approx -g_{F=2}$, see Section 2.6 (the difference is below the percent level). As shown in Fig. 3.2 (a), all atoms in the $|F = 1, m_\mathrm{F} = -1\rangle$ component are transferred globally to $|F = 2, m_\mathrm{F} = -1\rangle$ by a MW pulse and hold there for a fixed duration. Consequently, the condensate phases $\varphi_{\pm 1}$ now undergo Larmor precession with the same orientation, but the phase difference to φ_0 is changed in a magnetic bias field $B_Z(x)$. During the hold time τ, the spinor phase φ_S is locally advanced by $\Delta\varphi_\mathrm{S} \sim \Delta B(x)\tau$. The spatial profile of the spinor phase is therefore directly proportional to the sequentially applied intensity profile (Fig. 3.2 (b)), and the global offset value of the spinor phase is adjusted by the hold time. After the local phase imprint, all atoms are transferred back from $|F = 2, m_\mathrm{F} = -1\rangle$ to $|F = 1, m_\mathrm{F} = -1\rangle$. This method allows to imprint any form in the spinor phase. While illuminating one half of the condensate sequentially, this results in a sine-Gordon soliton in the spinor phase φ_S and a dip in the transverse spin length $|F_\perp|$, shown in Fig. 3.2 (c). As the imprinting of the phase happens on the time scale of the linear Zeeman shift, which is roughly 700 kHz at the applied bias field, the hold duration is shorter than one millisecond for all experiments reported in this thesis, which renders it stable against slow magnetic field fluctuations.

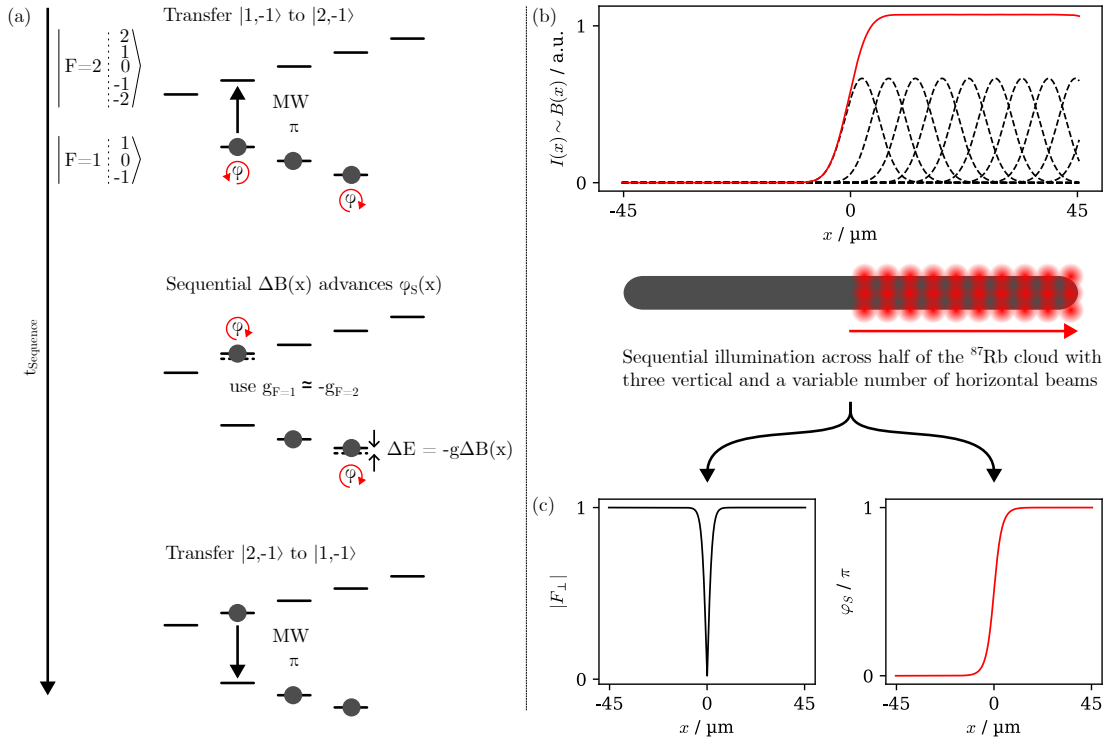

Figure 3.2: Scheme for the experimental preparation of a sine-Gordon soliton: (a) To advance the spinor phase as the phase difference between $|F = 1, m_\mathrm{F} = 0\rangle$ and $|F = 1, m_\mathrm{F} = \pm 1\rangle$, the opposite sign of the g-factor in $F = 1$ and $F = 2$ is used. Therefore, the complete population in $|F = 1, m_\mathrm{F} = -1\rangle$ is transferred to $|F = 2, m_\mathrm{F} = -1\rangle$ with a microwave pulse. Holding the atoms in this configuration allows to add locally an additional B-field by using the vector Stark shift, which advances the spinor phase proportional to the intensity of the laser beam. This is done sequentially over one half of the ^{87}Rb cloud, as shown in (b). Then, the population in $|F = 2, m_\mathrm{F} = -1\rangle$ is transferred back to $|F = 1, m_\mathrm{F} = -1\rangle$. (b) Since the vector Stark shift is proportional to the intensity of the laser beam, the single beams can be added up close to a sine-Gordon soliton profile, (c) resulting in a π kink in the spinor phase and a dip in the transversal spin length $|F_\perp|$.

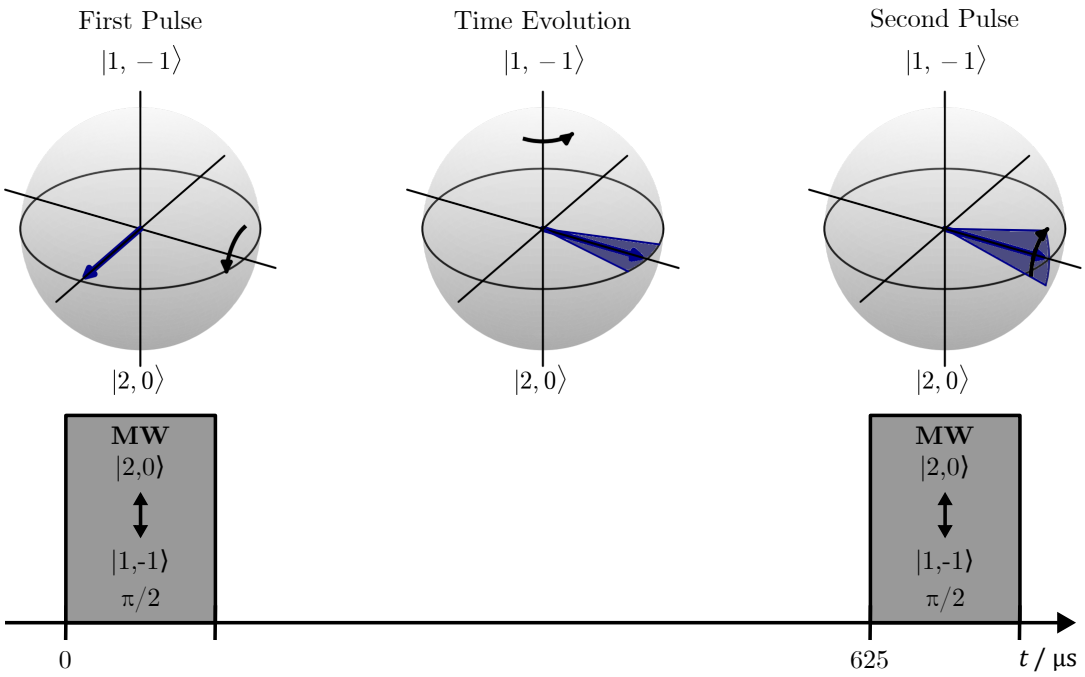

Figure 3.3: Ramsey Sequence to measure the fluctuation of the magnetic field stabilization: First, a $\pi/2$ RF pulse transfers half of the population from $|1,-1\rangle$ to $|2,0\rangle$. After a fixed duration of $\tau_R = 625$ μs, a second pulse rotates the system again. Ideally, the spin axis should now align with the rotation axis, but magnetic field fluctuations causes noise, which can be measured in the imbalance of the populations $N_{2,0} - N_{1,-1}$.

3.1.3 Imaging

Far-above saturation absorption imaging is used to capture the density distribution of the atoms after the readout pulse sequence. First, a magnetic field gradient pulse is applied with the coils of the magnetic trap, then, after a short time-of-flight of 2 ms, a resonant light pulse to $F = 2$ is imaging these states on one picture of a CCD camera. The atoms in $F = 2$ are also removed from the focal plane via this light pulse. Subsequently, a light pulse from the repumping laser transfers atoms from $F = 1$ to $F = 2$, which are then resonant to the $F = 2$ imaging light, captured on a second picture. Two more pictures are taken with the imaging light on, but ideally without any atoms, and a fifth picture is used as a dark noise reference. For further details see [41, 23].

3.1.4 Magnetic field stability

The stability of the magnetic field is crucial for precise state preparation, dressing and readout. To control the stabilization and set a precision level for the magnetic error of the quadratic Zeeman shift q_B, a Ramsey interferometry sequence is used between the states $|F = 1, m_\mathrm{F} = -1\rangle$ & $|F = 2, m_\mathrm{F} = 0\rangle$, shown in Fig. 3.3. Therefore, the imbalance

between $|1,-1\rangle$ & $|2,0\rangle$ is measured:

$$N_{1,2}^{-}/N = \left(N_{2,0} - N_{1,-1}\right)/N = \cos\delta_R \cdot \tau_R \,. \tag{3.1}$$

τ_R is the Ramsey time and δ_R the detuning from resonance. The sequence is performed with a $\pi/2$ MW pulse between $|1,-1\rangle \leftrightarrow |2,0\rangle$ with a small detuning $\delta_R = 2\pi\cdot 400$ Hz. Since the detuning is small compared to the Rabi frequency, the difference in the imbalance is negligible. But during the free time evolution, a phase shift is evolving between the state and the MW pulse. The Ramsey time $\tau_R = 625$ μs is chosen such that the spin is aligned with the rotation axis at the time of the second MW pulse, which should therefore not affect the imbalance. A difference in the population evolves by a difference in the detuning caused by magnetic field fluctuations. The detuning depends on the energy difference between the two levels, which is given in Eq. (2.31). The main contribution is the linear Zeeman shift of the $|1,-1\rangle$ level, therefore $\sigma_{\delta_R} = -g_{1,1}\sigma_B$ and the error of the magnetic field σ_B is calculated by

$$\delta_R = \frac{\arccos\left(N_{1,2}^{-}/N\right)}{2\pi\tau_R} \quad \Rightarrow \quad \sigma_B = \frac{\sigma(N_{1,2}^{-}/N)}{\sqrt{1-(N_{1,2}^{-}/N)^2}\, 2\pi\tau_R \cdot g_{1,1}} \,. \tag{3.2}$$

The error in the quadratic Zeeman shift is then given as $\sigma_{q_B} = 2g_{2,1}B_Z\sigma_B$, while the magnetic field strength $B \approx 0.894$ G is kept equal to the other measurements.

3.2 Local microwave transition

During the ongoing measurements regarding the sG wave packets, a tool could be established, which allows local manipulation in the MW regime. The work of the bachelor's thesis by Suelberg [42] follows hereby previous work of Doering et al. [8]. MW transitions are to this point only possible for the total BEC and used to transfer atoms between the hyperfine levels, for example during the spinor phase imprint described in Section 3.1.2. This is done via radiating the condensate with microwaves from an antenna located next to the experimental chamber, also seen in Fig. 3.1. A more direct approach to the preparation of the spinor phase and opening up further possibilities for future experiments could be done via Raman transitions, where laser light is modulated in the MW range. An electro-optical modulator (EOM) from *EOspace* is used to modulate the same local laser beam used for the local imprint described in Section 3.1.2. Since the EOM uses phase modulation, which cannot be used directly to drive Raman transitions, it must be converted into amplitude modulation. For this an interferometer setup is used: a stable solution is the Sagnac interferometer because of the traveling light passing the setup in both directions on a round trip. Since the traveling-wave EOM modulates only in one direction, the interference at the output cancels the unmodulated carrier frequency with the zeroth component of the modulated beam and leaves the modulated frequencies unchanged. These modulated light beams with $\omega_\pm = \omega_0 \pm \omega_{MW}$, where ω_0 is the unmodulated light frequency and $\omega_{MW} = \omega_{(1,m_\mathrm{F})\leftrightarrow(2,m_\mathrm{F})}/2$ is half the transition frequency between two hyperfine levels of the $F=1$ and $F=2$ manifold, can drive a localized Raman transition with the precision of the local laser beam. For more details on the setup itself see [42]. The final test of the setup was done in the BEC apparatus, where it was

installed temporarily in the beam path of the local imprint. The transition frequency was set to $\omega_{MW} = \omega_{(1,0)\leftrightarrow(2,0)}/2 = 2\pi \cdot 3.417$ GHz, also taking energy shifts like the second order Zeeman shift into account.

4 Experimental results

In this chapter, the experimental results are presented. First, the characteristics of the magnetic field stabilization and the local imprint are tested. Then, the validity of the new readout sequences is discussed, before the measured details of the sine-Gordon soliton dynamics are shown. In the end, a measurement with the local MW control is shown and analyzed.

4.1 Magnetic field fluctuations

Stability of the magnetic offset field is crucial for both the quench experiments and the readout sequences. State manipulation from the MW pulses is dependent on the Zeeman shift as well as the dressing q, which is only in the order of Hz. Therefore, one of the first steps is to measure the fluctuations in the magnetic field stabilization using a Ramsey sequence between $|F = 1, m_\mathrm{F} = -1\rangle$ and $|F = 2, m_\mathrm{F} = 0\rangle$, as introduced in Section 3.1.4. The time between the two Ramsey pulses is kept constant such that the population is half in each level, which means that the imbalance $N^-_{1,2}$ from Eq. (3.1) between these two states should be zero. Indeed, the fluctuation is around zero, as Fig. 4.1 shows. Plugging in the standard deviation of the measurement into Eq. (3.2), one finds a fluctuation of $\sigma_B = 17\ \mu$G at a magnetic field of $B = 0.894$ G. This results in a precision of $\sigma_{q_B} = 2.2$ mHz with the magnetic quadratic Zeeman shift of $q_B = 57.5$ Hz. This is in the per mille order of magnitude of the the actual tuned quadratic Zeeman shift $q = q_B - q_{MW} \sim 1$ Hz, described in Section 3.1. Since the fluctuations on the effective shift q are in the order of magnitude of $\sigma_q \sim 0.2$ Hz [21], the magnetic field control provides a stable basis for the precision needed for preparing the sG solitons.

4.2 Calibration of the readout phases

The phases of the RF and MW pulses drift during the experiments in the time scale of days to weeks. In order to measure the right observable, the phases have to be calibrated regularly. For both new readout sequences, three phases have to be determined: the spinor phase during the preparation, the phase imprint between F_x and Q_{yz} in the end of the sequence and the orientation that is given by the phase of the RF pulses in order to rotate the system around the right axis. As described in Section 3.1.1, the spinor phase during the preparation must be calibrated to reach maximal transversal spin. In the usual readout for $F_\perp$ and also for the other sequences, this is done via a scan of the MW pulse phases in the arbitrary waveform generator (AWG). Fig. 4.2 (a) shows a fit of the absolute of a sine function $(a \cdot |\sin(bx + c)| + d)$, where the phase value of the maximum of $|F_\perp|$ is used. Then a scan of the RF orientation is done, which is a total offset on the RF phase for F_x as well as on F_y. Fig. 4.2 (c) shows a measurement with a total elongated spin, which should point in F_x direction. This is not only important for the rotation around the right axis, but also to fulfill the operator commutation relation discussed in Section 2.2.

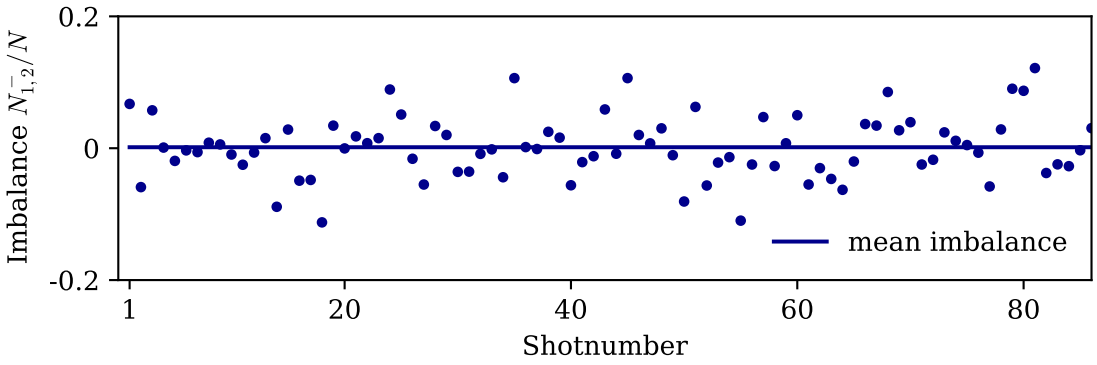

Figure 4.1: Magnetic field fluctuations: crucial for the control of the dressing is the stability of the quadratic Zeeman shift q_B. For this, the Imbalance was measured as described in Section 3.1.4. The deviation in the Imbalance results in magnetic field fluctuations of $\sigma_B = 17$ μG at a magnetic field of $B = 0.894$ G and a precision of $\sigma_{q_B} = 2.2$ mHz.

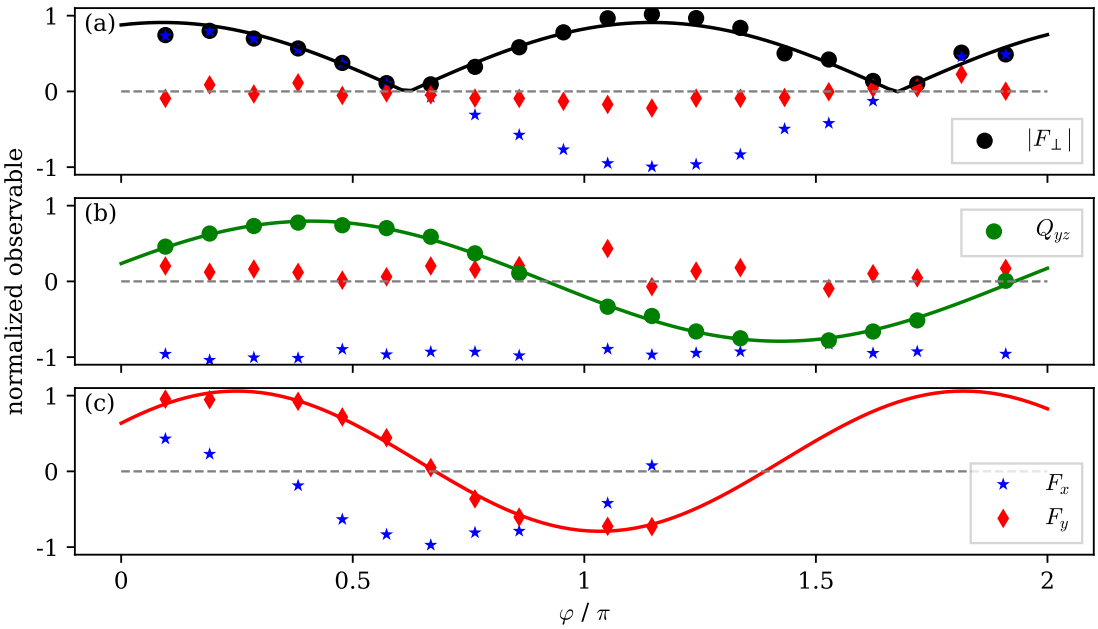

Figure 4.2: Phase calibration for the readout sequences: (a), the measurement is shown for the initial spin length calibration by scanning the relative MW phase. (b) shows the variation of the MW pulse imprint phase at the end of the sequence, where the spin should be aligned along F_x and $Q_{yz} = 0$. (c) For the RF rotations is a total offset phase added to the F_x and F_y rotation pulses to align the rotational axes with the desired ones, as depicted in Fig. 2.2.

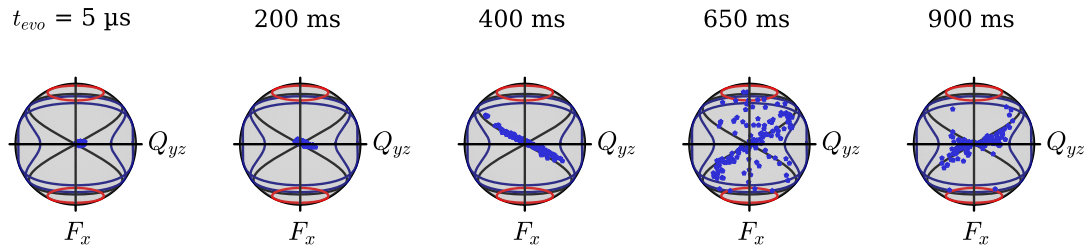

(a) This measurement shows polar quench dynamics with the re-implemented spinor phase readout established by Kunkel et al. [22]. Here, the data is limited to the spin-nematic equator.

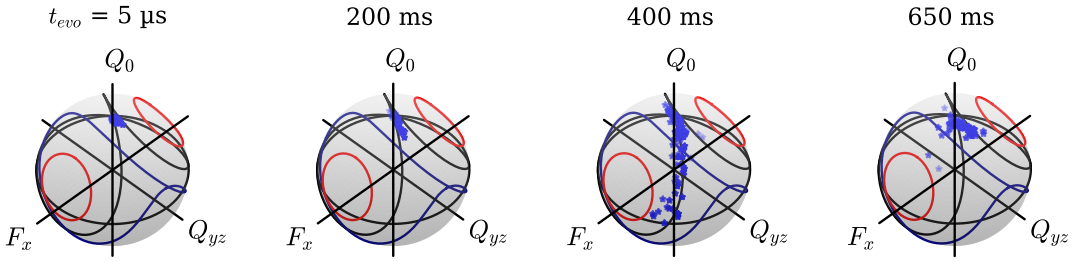

(b) This measurement shows again polar quench data, but with the full spin-nematic readout. This allows to track the quench dynamics on the entire spin-nematic sphere.

Figure 4.3: The Polar quench measurements are done in the XDT, where the single mode dynamics are used as a benchmark to verify the new readout sequence [21]. (a) shows a re-implementation of the F_x-Q_{yz} readout in the spin-nematic equator only and (b) shows the expansion in the entire spin-nematic sphere. The initial polar state is on top of the sphere with $Q_0 = 1$, then follows the separatrix, which is seen after an evolution time of $t_{evo} = 400$ ms. During the last two times, the state re-focuses at Q_0.

Therefore, the value is taken where $F_y = 0$. Finally, a measurement varying the phase of the second MW imprint pulse is done to align Q_{yz} to zero as well. Fig. 4.2 (b) shows this calibration measurement, where Q_{yz} varies as the imprint pulse phase is changing, but F_x and F_y are constant.

4.3 Verification of the spin-nematic readout sequence

The first step was the re-implementation of the spinor phase readout established by Kunkel et al. [22]. One good physical process to verify the readout is the spin mixing process described in Section 2.6.1. The experiment is done in the XDT to ensure single mode dynamics, where it is known how a state evolves [21]. Since the spin mixing is independent of the Larmor phase rotation and conserves the total magnetization (and therefore F_z), the dynamics is constrained to the spin-nematic sphere. The polar state is initially prepared at the center of the separatrix. Then, the system is quenched from the polar phase into the EP phase by applying the off-resonant MW dressing[1]. During the time evolution, the state will be dragged along this line, which can be seen after $t_{evo} = 400$ ms in

[1] That is why the experiment is called "polar quench".

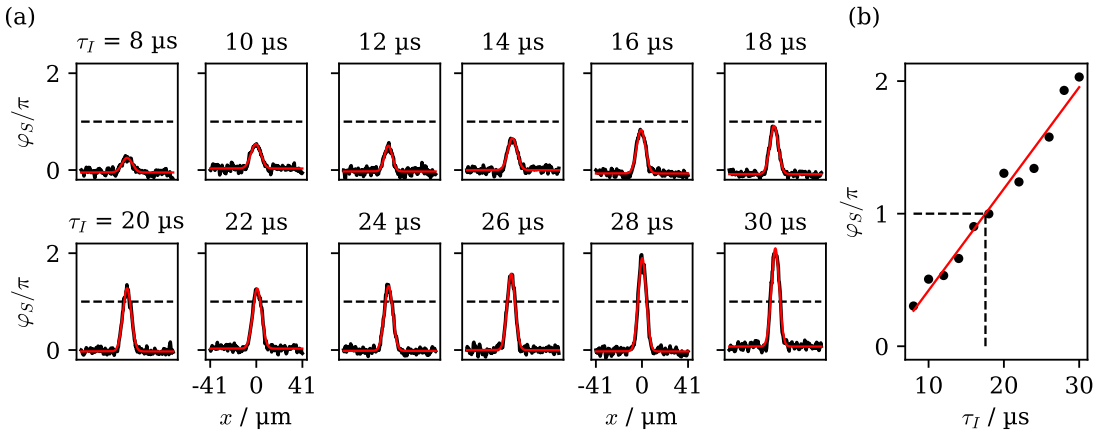

Figure 4.4: (a) To calibrate the necessary illumination time in order to rotate the spinor phase to $\varphi_S = \pi$, a horizontal Gaussian profile was imprinted on the condensate with three vertical beams with variable beam time τ_I, as described in Section 3.1.2. A beam width of $\sigma = (7.6 \pm 0.6)$ μm could be determined. (b) The amplitudes are plotted against the imprint time τ_I. A π rotation time could then be determined via a linear fit to $\tau_I(\varphi_S = \pi) = (17.6 \pm 0.1)$ μs.

Fig. 4.3 (a). The dynamic will evolve fast along the separatrix, so for $t_{evo} = 650$ ms the state already re-focuses in the center. In the single-mode mean-field picture, the entire condensate undergoes this coherent evolution where one point in the figures corresponds to one measurement of the entire BEC. Since this process is statistical in character, multiple measurements had to be taken in order to get an estimate of the full F_x-Q_{yz} distribution. For the next step of expanding the spinor phase readout to a full spin-nematic readout introduced in Section 2.5.1, the polar quench also is handy due to the fact that the interaction stays on the spin-nematic sphere. Fig. 4.3 (b) shows the initial condition at the shortest evolution time measurable with the apparatus. This lays right at the north pole with maximal Q_0 expectation value. After the quench, the state undergoes the same time evolution on the sphere and re-focuses at the north pole. One effect not visible in Fig. 4.3 (b) is the intrusion of some measurements into the sphere. This can be explained by a drift in the Larmor phase due to imperfect offset magnetic field compensation. This can rotate the state on the spin sphere, causing a reduction of the state length on the spin-nematic sphere. Nonetheless, the polar quench experiment showcases the functionality of the new readout sequence and can be used further in the ongoing measurements regarding the sG soliton and breather.

4.4 Local imprint characterization

It is crucial for any experiments to prepare the system in the correct initial condition. For the experiments described hereafter, a local spinor phase imprint is employed. While the depth and form was measured previously indirectly in the observable $|F_\perp|$ by Klein [18], it was now possible to measure the spinor phase rotation directly. As mentioned in Section 3.1.2, the rotation is dependent on the light intensity and illumination time. To

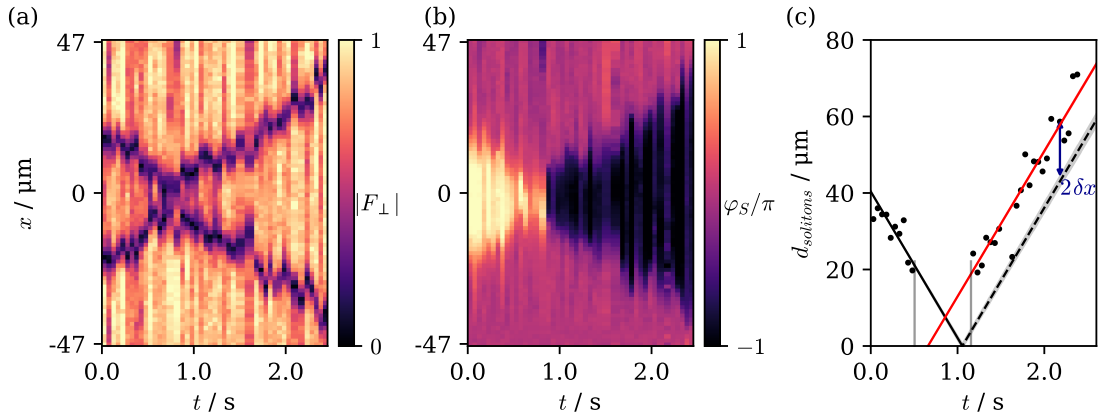

Figure 4.5: K-$\bar{K}$ collision captured simultaneously in the observables $F_\perp$ (a) and φ_S (b). From the two dips in $F_\perp$ was the velocity and distance before and after the collision extracted, from which the phase-shift $\delta x = (7.51 \pm 0.47)$ μm could be calculated (c). A flip in the spinor phase was also captured in (b) and compared to the theory in Fig. 4.6.

calibrate the necessary imprint time τ_I, three vertical beams and one in the horizontal direction illuminate the condensate. This is done because it is the same configuration as used in the soliton experiments reported later in Sections 4.5 and 4.6. The initial condition was measured right after the preparation with 5 μs evolution time, which is the shortest experimentally accessible time. Fig. 4.4 (a) shows the resulting rotations for imprint times between 8 and 30 μs with fixed intensity. The width of the Gaussian profile could then be fitted to a mean value of $\sigma = (7.6 \pm 0.6)$ μm, which is in accordance with the measured waist from Lannig [23] after installation ($\sigma = (7.0 \pm 0.3)$ μm). Fig. 4.4 (b) shows the amplitudes of the fits against the imprint time, where $\tau_I(\varphi_\mathrm{S} = \pi) = (17.6 \pm 0.1)$ μs for a π-rotation could be determined. This is then used as a reference to create a continuous and flat spinor phase profile as an overlap of multiple horizontal beams, as in Section 3.1.2 described, or to form the initial function of a breather. While the system is stable in the preparation of a soliton regarding the rotation of $\varphi_\mathrm{S} \approx \pi$ and adjusts itself, the preparation of a breathing solution is strongly dependent on the initial condition, discussed in Section 4.6.

4.5 Sine-Gordon soliton

As discussed in Section 2.7, the spinor BEC can in some approximation be well described by a LEEFT, taking the form of a sG equation in the spinor phase φ_S for $q = 0$ [37]. This makes it particularly interesting to study their dynamics. One interesting excitation of the system out of the equilibrium is the sG soliton, which is a prominent solution of the sG model [5]. It interpolates between two minima in the EP potential, as depicted in Fig. 2.5 (b). To test whether the soliton originates from the sG theory, it must not only take the same functional form [7], but also exhibit elastic interaction, since the model is integrable. To show these theoretically predicted phenomena, a kink and anti-kink collision is prepared. The sG soliton kink in the spinor phase results in a dip in the transversal spin length $|F_\perp|$. Since the Larmor phase is random in each measurement,

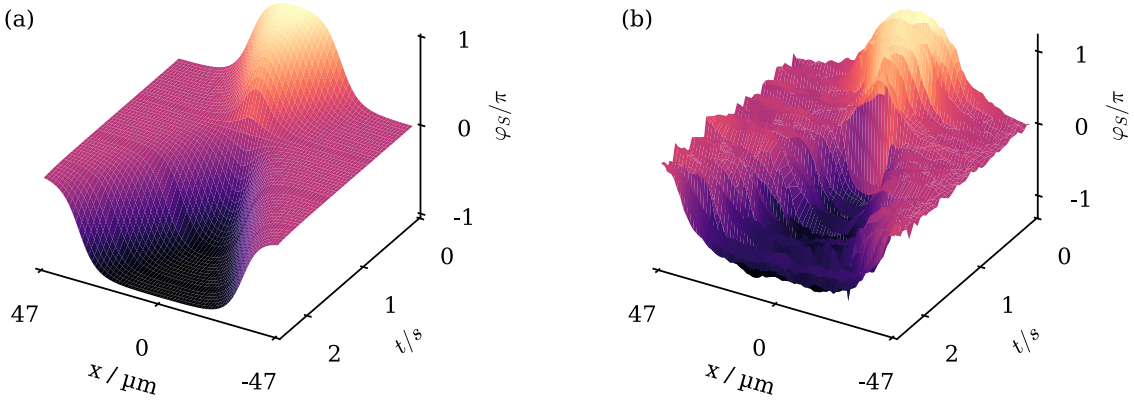

Figure 4.6: The collision of a kink and anti-kink shown in the spinorphase from theory (a) and the event captured in the experiment (b). The units for conversion are extracted as described in Section 4.5 and $q = 0.7$ with a starting distance of $d = 36.5$ μm.

the signal in the $F_\perp$ readout from Kunkel et al. [22] is clear in every realization, but the spinor phase measurement discussed in Section 4.3 has to be post selected in this measurement for a clear signal. Both observables has been measured separately with the previous readouts, but to extract the soliton behavior simultaneously in both observables, the dual-phase readout (DuPR) was developed and implemented. This comes at the cost of increased noise, therefore it was first shown that the signal can reproduce previous results from separate $F_\perp$ and spinor phase readout measurements as a verification. With this tool, it was possible to resolve a controlled K-$\bar{K}$ collision, Fig. 4.5 shows the complete DuPR measurement. One exemplary time slice of the $|F_\perp|$ profile and simultaneously captured spinor phase can be seen in Fig. A.1. The velocity can be controlled via the MW dressing q, where $v(q = 0) = 0$. $q = 0.7$ Hz was chosen such that the elasticity is close to unity, which is one condition for a pure sG theory. The analysis in Fig. 4.5 (c) is done with a fit on the $|F_\perp|$ profile for each time slice in Fig. 4.5 (a)

$$|F_\perp|(x) = \left| a_1 \tanh\left(\frac{x - x_1}{\ell}\right)\right| + \left| a_2 \tanh\left(\frac{x - x_2}{\ell}\right)\right|, \tag{4.1}$$

where a_i, x_i are the amplitudes and positional shifts, respectively. The mass and the speed of sound was absorbed into the parameter ℓ, which is introduced here as the length scale of the solitons. The mean width of the solitons is determined to $\ell = (5.98 \pm 0.37)$ μm. Experiments as well as numerical simulations showed a constant width of the soliton regardless of their velocity for the spin-1 system with a connection of $l = \xi_s/\sqrt{2}$ [7]. At the moment, the density was not measured in the experiment, but with the connection to the soliton length scale, the spin healing length could be determined to $\xi_s \approx 8$ μm. From Siovitz et al. [37], also the time scale can be deduced to $T = 2M\xi_s^2/\hbar = 4M\ell^2/\hbar = (197 \pm 24)$ ms. This provides a good approximation for the length and time scale between the experimental and theoretical values. The analysis of the velocities reveals an elasticity of $v_{out}/v_{in} = (0.99 \pm 0.02)$, which fulfills one necessary condition. It must be mentioned here that the data in Fig. 4.5 is composed of four individual runs, which is necessary to pick a clear signal in the spinor phase. Although

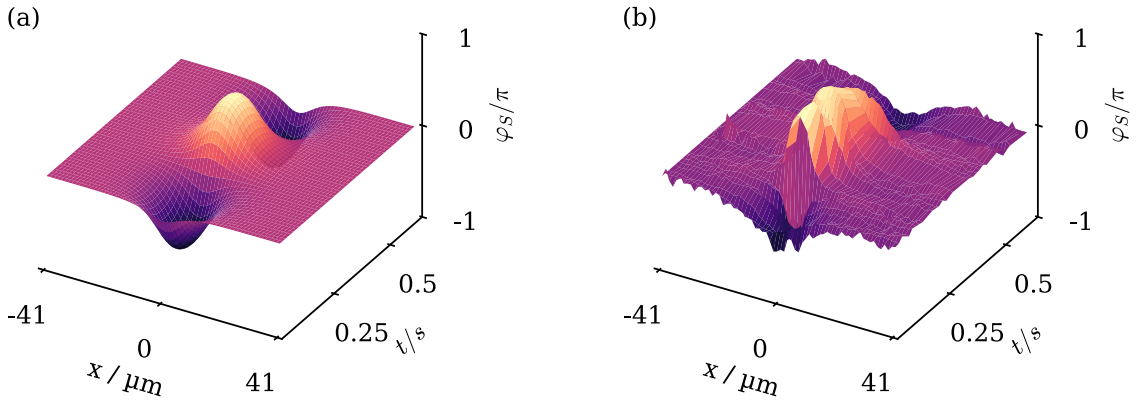

Figure 4.7: Comparison of the theoretical breathing solution (a) with a measurement (b). The parameters for conversion between units were found by a fit described in Section 4.6, with $\ell = (4.89 \pm 1.43)$ μm and $T = (132 \pm 77)$ ms

one must be careful with the velocity extraction of this measurement, the width of the solitons and overall qualitative characteristic in the phase is reliable. The phase jump in φ_S of 2π can be seen in Fig. 4.5 (b), which is theoretically predicted and illustrated in Fig. 4.6. The last predicted value is the positional shift δx of each soliton ahead in the propagation direction. Fig. 4.5 (c) shows the distance between the kink and anti-kink. The shift ahead of each soliton corresponds to double the phase shift in the distance, which could be calculated to $\delta x_{exp} = (7.51 \pm 0.47)$ μm. The theoretical positional shift is, following Eq. (2.45) with the extracted velocity and applied q, $\delta x_{theo} = 13.41$ μm. But the theoretical value is not expected to fit quantitatively, since effective theory is not applicable during the collision. The collision exhibits the full spin-nematic sphere and thus violates the underlying assumptions from Siovitz et al. [37]. This is similar to the other sG solution, the breather, which can be seen as a bound state of a kink and anti-kink, discussed in the following Section 4.6. These results are consistent with the other measurements taken during the project [7].

4.6 Sine-Gordon breather

After establishing and characterizing the experimentally generated sG solitons, there is another excitation unique to the sG model: the breather, which is a solution localized in space and periodic in time. In the analytical solution of Eq. (2.41), the width and breathing frequency are determined only by the amplitude μ. But the experimental system features its own length scale, the spin healing length ξ_s. This makes it particularly difficult to match the initial solution to a stable oscillation. The initial imprint is done similar to the soliton solution mentioned in Section 3.1.2 and calibrated described in Section 4.4. It was possible to capture a breathing solution similar to the analytical model. Fig. 4.7 shows the comparison. For a system prepared at $q = 0$, Q_0 is expected to be globally stable. However, by using the full spin-nematic readout, the measurement revealed also an oscillation in the third dimension of the spin-nematic sphere, as shown in Fig. 4.8 (a). This

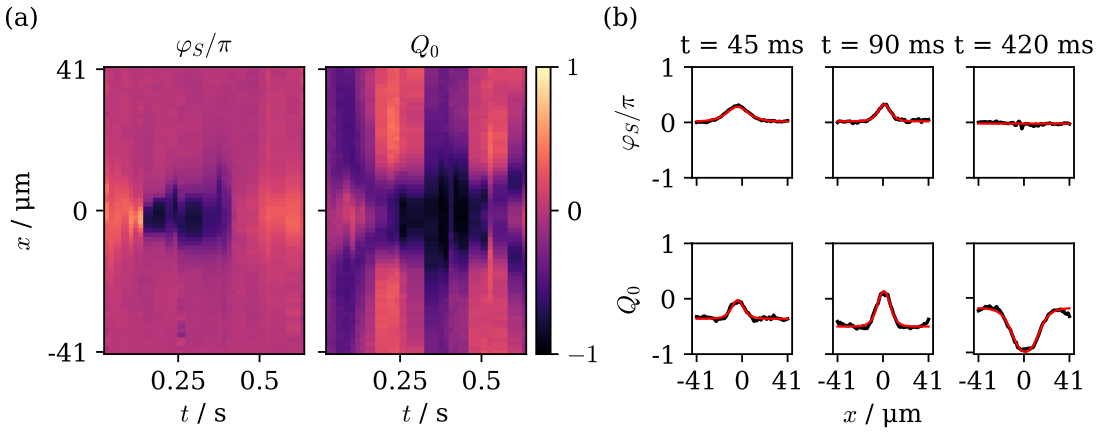

Figure 4.8: (a) Breathing solution in φ_S and Q_0. The background oscillation is emerging as the initial condition was not set perfectly, which could be confirmed via numerical GPE simulations. (b) Time slices of the breathing solution: the analytical form of a breather could be fitted to this measurement in the spinor phase as well as in Q_0.

oscillation has the same frequency, but has a phase shift of $\pi/2$. This can be understood as a rotation around the spin-nematic sphere, which could be confirmed by numerical GPE simulations. Another interesting phenomenon of the Q_0 oscillation is the oscillation in the background. Again, the expectation would be a flat signal on each side of the breather, but there is also an oscillation emerging due to imperfect initial conditions. This behavior could also be confirmed by numerical simulations. The analytical form for a single time slice could be fitted in Fig. 4.8 (b), with the amplitude μ, the interaction strength parameter $g = 2$ and an added length scale ℓ as fit parameter in Eq. (2.41):

$$\varphi(x,t) = \frac{4}{g\pi} \arctan\left((\tan\mu) \frac{\sin(\chi\cos\mu)}{\cosh(Z\sin\mu)} \right), \quad \chi \equiv \frac{t}{T} + \chi_0\,, \quad Z \equiv \frac{x - vt - x_0}{\ell}\,. \tag{4.2}$$

$T = 2M\xi_s^2/\hbar$ is the time scale determined in Section 4.5 and χ_0 the initial phase shift. An imprint depth of $\mu = (0.32 \pm 0.14)\ \pi$ could be determined for all times shown in Fig. 4.8 (b), the mean width is $\ell = (4.89 \pm 1.43)\ \mu$m. What could be captured in the third slice in Fig. 4.8 (b) is the complete rotation of the spinor phase into Q_0.

4.7 Local microwave manipulation

The local microwave setup described in Section 3.2 was tested to drive transitions between a pseudospin-$1/2$ system of $|F = 1, m_F = 0\rangle$ and $|F = 2, m_F = 0\rangle$ sublevels. The system was therefore prepared in the polar ground state inside the box walls as for the soliton experiments. In the first test, one beam was illuminating the middle of the BEC with gradually increasing duration to drive locally confined Rabi oscillations, as shown in Fig. 4.9 (a). The population transfer to $F = 2$ follows the theoretical Rabi oscillation $P_{1,0} = A\cos^2(\Omega t/2 + \varphi_0) + d$ with amplitude A, phase shift φ_0 and offset d. In Fig. 4.9 (b) is a slice from the middle of the BEC shown, where the oscillation could be fitted to.

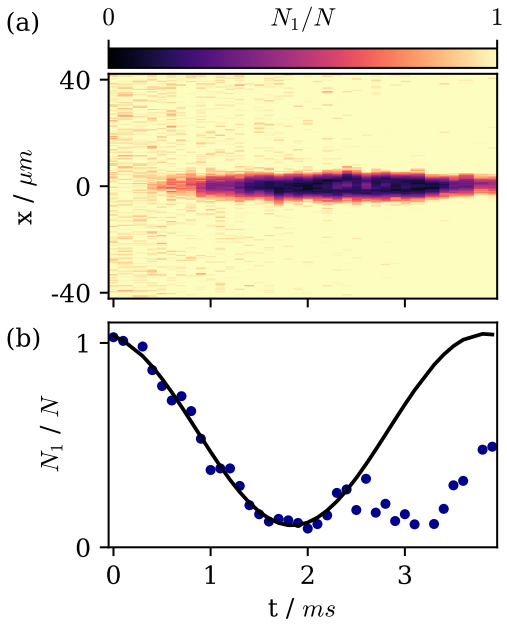

Figure 4.9: (a) An effective local MW Rabi oscillation could be driven using a modulated laser. In (b) is a fit of $x = 0$ to find the time for a $\pi/2$ pulse. Illumination times $t < 2.5$ μs are used to exclude effects from the Gaussian intensity distribution.

Since the laser beam has a Gaussian intensity distribution and the oscillation frequency in the Jaynes-Cummings model being dependent on the intensity [14], the transfer back to $F = 1$ starts in the center at ~ 2 ms, but the atoms are caught by the surrounding ones, where the intensity is less. For this transition a Rabi frequency of $\omega_R = 2\pi \cdot (252 \pm 12)$ Hz was found, which corresponds to a full transition time of $\tau_{\pi/2} = (1.98 \pm 0.10)$ ms. This is unfortunately too long to use it for the spinor phase imprint to be stable against magnetic field drifts. The current preparation time is ~ 650 μs for multiple beams, which is shorter than the linear Zeeman timescale, as described in Section 3.1.2. It is interesting though to test the dynamics of the mixture after preparing a $F = 2$ wave packet in a background of surrounding $F = 1$ atoms. This is shown in Fig. 4.10. One modulated laser beam illuminated the middle of the BEC for a fixed imprint duration of $\tau_I \in \{1.5, 1.8, 2.0, 2.2\}$ ms, afterwards the time evolution of the created wave packet was measured deep in the polar phase. This means that the zero component is favored in both hyperfine states, resulting in conserved absence of magnetization. For $\tau_I < \tau_{\pi/2}$, the initial wave packet disperses and creates phononic excitations on the BEC. Close to an initial preparation of the wave packet fully to $F = 2$, two dark-bright solitons are created with a dip in the $F = 1$ density and a bump in $F = 2$. They split apart and travel in opposite directions while keeping their shape for $\tau_I > \tau_{\pi/2}$. Fig. 4.10 shows the bright wave packet in $F = 2$. For $\tau_I = 2.2$ ms, the form could be fitted to the shape of two solitons following [2, 30]

$$n(x) = \sum_{i=1,2} \frac{1}{\gamma_i^2} \mathrm{sech}^2\left(\frac{x - x_i}{\gamma_i \ell_i}\right), \qquad \gamma_i = \left(1 - \left(\frac{v}{c_i}\right)^2\right)^{-\frac{1}{2}}, \tag{4.3}$$

with γ_i, l_i, x_i, c_i being the relativistic factor, the width, the positional shift and the sound velocity of the two peaks. One exemplary time slice of the fit can be seen in Fig. A.2. First, the positional shift was extracted to determine the velocity to $v = (210 \pm 7)$ μm/s. Then this value was inserted in Eq. (4.3) to fit the width and the sound velocity. The

width corresponds to the one-dimensional healing length and could be determined to $\xi = \ell = (2.34 \pm 0.27)\ \mu$m and the sound velocity is $c = (346 \pm 69)\ \mu$m/s. These values are consistent with $\xi = \frac{\hbar}{mc}$ within the error bars [2]. Here it can also be mentioned that the generated solitons do not have a magnetic character, but are polar, which means that they differ significantly from solitons that have been investigated in other scenarios [11, 27, 28, 33, 4]. However, the interaction can be driven through the scattering between atoms: the intraspecies scattering lengths in ^{87}Rb are of the same magnitude with $a_{11} = 100.4\, a_B$, $a_{22} = 95\, a_B$, and the interspecies scattering length is close to the miscibility-immisciblity threshold $a_{12}^2 = a_{11}a_{22}$ with $a_{12} = 97.7\, a_B$ [19, 27, 28]. The proximity to this threshold can explain the emergence of solitons at an imprint depth around the Rabi time, at which a large number of particles occupy $F = 2$. The behavior of stable soliton generation under these conditions has already been reported in [2], if the extent of the soliton is greater than the healing length. This is satisfied, since the extend of the soliton is enlarged through the relativistic γ factor. In the last panel in Fig. 4.10 are the sound velocity in red lines extracted from the fit and, in white, the velocity of the solitons added. Also visible is the reflection of the wave packets at the box walls. The interaction is not fully elastic but the solitons accelerate afterwards, still with a velocity less than the sound velocity c. The left soliton gathers more energy from the interaction with a velocity of $v_{l,out} = (293 \pm 38)\ \mu$m/s, corresponding to a reflectivity of $v_{l,out}/v_{l,in} = 1.43$. The right soliton has a reflectivity of $v_{r,out}/v_{r,in} = 1.27$. The mean velocity after the reflection is $v_{out} = (283 \pm 32)\ \mu$m/s.

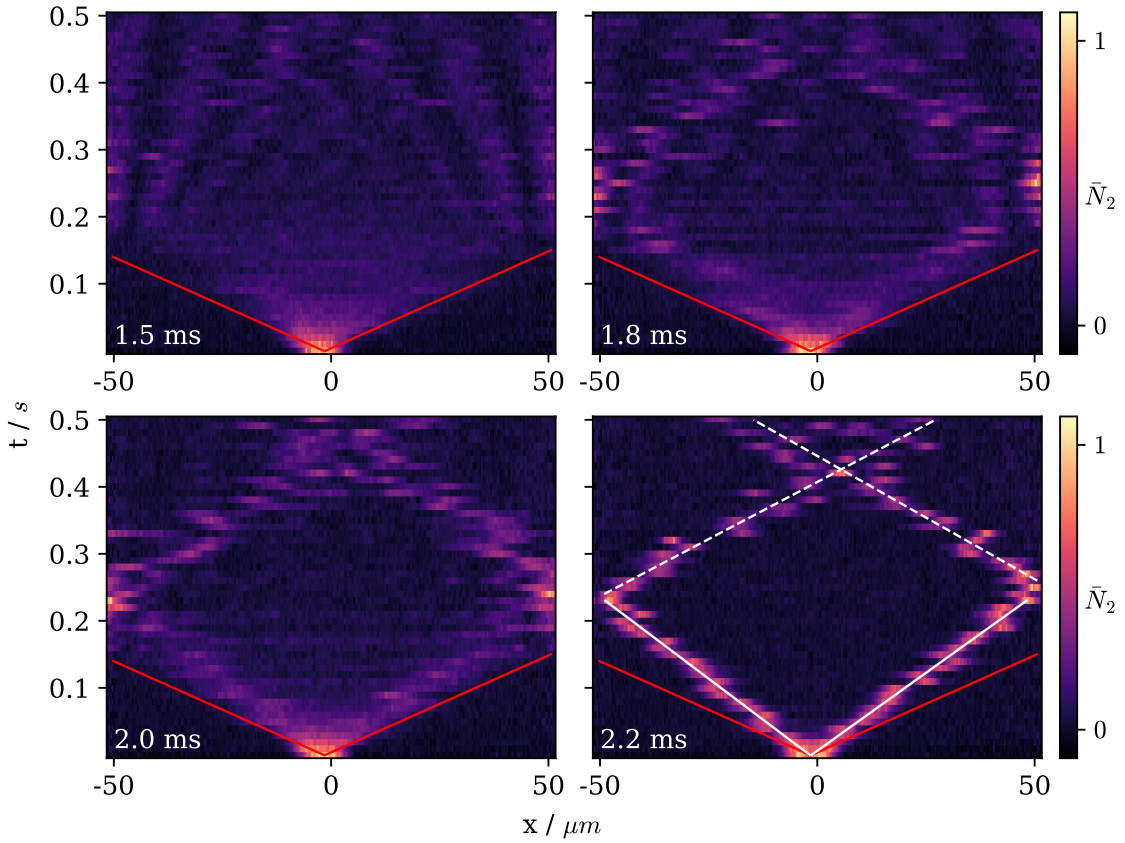

Figure 4.10: For the final test of the local MW setup, the population in $F = 2$ was altered with different imprint times around the full transfer time. For a low atom population, the wave packet disperses and creates phononic waves, while for a deeper imprint, a dark-bright soliton emerges. From a fit, the velocity in white and sound velocity in red could be extracted, as well as an interaction with the box walls.

5 Conclusion

The aim of this thesis was first to provide the current project with tools for measuring the necessary non-commuting observables in order to gather information about the dynamics of the condensate [7]. Two new readout sequences could be established and shown to capture the right observables. With these tools, first the initial local spinor phase imprint could be calibrated by direct measurement of the spinor phase. That a ^{87}Rb Bose-Einstein condensate exhibits a sine-Gordon model was already predicted and reported from Siovitz et al. [37], but the observation of the in-situ structure and dynamics of their solutions, like a breather (Section 4.6) and a sG soliton (Section 4.5) is now also possible with the help of the new readout tools. To show that the solitons arise from the sG model, it is essential that the collision behavior follows the predictions. The characteristics like a 2π jump and the spatial phase shift could be observed in a kink and anti-kink collision. In beyond, the expectation for the dual-phase readout was to measure the spinor phase without post selection by rotating the observables according to the simultaneously detected Larmor phase. Unfortunately, this expectation could not be fulfilled. The spin-nematic sphere is only defined for a fixed Larmor phase, based on Section 2.2, as was later realized. Nonetheless, these tools are not only beneficial during the current project, but can also become handy for future experiments.

Second, a setup for localized transitions between the hyperfine states has been successfully tested. It can reliably change the populations in the MW range with a spatial resolution compared to the local spinor phase imprint measured in Section 4.4. The drawback is the low Rabi frequency, where the transition happens on too large a timescale for the desired application, so maybe the setup reported by Levine et al. [25] would be more suitable. However, the outcome of the final test is in accordance with the literature, where velocities of the generated solitons could be extracted. It was not further examined how to control the velocity, which can be up to future work, or testing the lifetime, since they are supposed to have long coherence times [19]. Further measurements could also explore the regime with MW dressing to enable spin-changing collisions on top.

Acknowledgment

Finally, I thank Markus for giving me the special opportunity to work in his group. The discussions and the work with him were very inspiring, and i always left the meetings with greater knowledge than before. Many thanks to Lauriane, who very kindly agreed to take part in the review. I would like to thank the team, who always supported me and answered all my questions in great detail, no matter how absurd they were. This applies not only to the BEC-team of Yannick, Alex and Raphael, but also to the entire experimental group and colleges from the theory department. It was a pleasure to work with Levi to build the local MW setup. Also the people from the workshop helped a lot during the build-up. At this point, special thanks to Helmut, who is a not only a walking encyclopedia, but also provided his exceptional experience in the laboratory. Many thanks also to Christiane and Petra from the administration, who helped a lot with every question i came up with. It was a really good time.

A Appendix

A.1 Spin-1 Operators

$$\hat{\mathcal{N}} = \mathbb{1}_3 = \begin{pmatrix} 1 & 0 & 0 \\ 0 & 1 & 0 \\ 0 & 0 & 1 \end{pmatrix} \qquad \hat{N} = \hat{a}_0^\dagger \hat{a}_0 + \hat{a}_{+1}^\dagger \hat{a}_{+1} + \hat{a}_{-1}^\dagger \hat{a}_{-1}$$

$$\hat{\mathcal{F}}_x = \frac{1}{\sqrt{2}} \begin{pmatrix} 0 & 1 & 0 \\ 1 & 0 & 1 \\ 0 & 1 & 0 \end{pmatrix} \qquad \hat{F}_x = \frac{1}{\sqrt{2}} \hat{a}_0^\dagger \Big(\hat{a}_{+1} + \hat{a}_{-1} \Big) + \frac{1}{\sqrt{2}} \Big(\hat{a}_{+1}^\dagger + \hat{a}_{-1}^\dagger \Big) \hat{a}_0$$

$$\hat{\mathcal{F}}_y = \frac{\mathrm{i}}{\sqrt{2}} \begin{pmatrix} 0 & -1 & 0 \\ 1 & 0 & -1 \\ 0 & 1 & 0 \end{pmatrix} \qquad \hat{F}_y = \frac{\mathrm{i}}{\sqrt{2}} \hat{a}_0^\dagger \Big(\hat{a}_{+1} - \hat{a}_{-1} \Big) - \frac{\mathrm{i}}{\sqrt{2}} \Big(\hat{a}_{+1}^\dagger - \hat{a}_{-1}^\dagger \Big) \hat{a}_0$$

$$\hat{\mathcal{F}}_z = \begin{pmatrix} 1 & 0 & 0 \\ 0 & 0 & 0 \\ 0 & 0 & -1 \end{pmatrix} \qquad \hat{F}_z = \hat{a}_{+1}^\dagger \hat{a}_{+1} - \hat{a}_{-1}^\dagger \hat{a}_{-1}$$

$$\hat{\mathcal{Q}}_{yz} = \frac{\mathrm{i}}{\sqrt{2}} \begin{pmatrix} 0 & -1 & 0 \\ 1 & 0 & 1 \\ 0 & -1 & 0 \end{pmatrix} \qquad \hat{Q}_{yz} = \frac{\mathrm{i}}{\sqrt{2}} \hat{a}_0^\dagger \Big(\hat{a}_{+1} + \hat{a}_{-1} \Big) - \frac{\mathrm{i}}{\sqrt{2}} \Big(\hat{a}_{+1}^\dagger + \hat{a}_{-1}^\dagger \Big) \hat{a}_0$$

$$\hat{Q}_{xz} = \frac{1}{\sqrt{2}} \begin{pmatrix} 0 & 1 & 0 \\ 1 & 0 & -1 \\ 0 & -1 & 0 \end{pmatrix} \qquad \hat{Q}_{xz} = \frac{1}{\sqrt{2}} \hat{a}_0^\dagger \Big(\hat{a}_{+1} - \hat{a}_{-1} \Big) + \frac{1}{\sqrt{2}} \Big(\hat{a}_{+1}^\dagger - \hat{a}_{-1}^\dagger \Big) \hat{a}_0$$

$$\hat{Q}_{zz} = \frac{2}{3} \begin{pmatrix} 1 & 0 & 0 \\ 0 & -2 & 0 \\ 0 & 0 & 1 \end{pmatrix} \qquad \hat{Q}_{zz} = \frac{2}{3} \Big(\hat{a}_{+1}^\dagger \hat{a}_{+1} + \hat{a}_{-1}^\dagger \hat{a}_{-1} \Big) - \frac{4}{3} \hat{a}_0^\dagger \hat{a}_0$$

$$\hat{\mathcal{Q}}_0 = -\hat{\mathcal{Q}}_{zz} - \frac{1}{3} \hat{\mathcal{N}} = \begin{pmatrix} -1 & 0 & 0 \\ 0 & 1 & 0 \\ 0 & 0 & -1 \end{pmatrix} \qquad \hat{Q}_0 = \hat{a}_0^\dagger \hat{a}_0 - \Big(\hat{a}_{+1}^\dagger \hat{a}_{+1} + \hat{a}_{-1}^\dagger \hat{a}_{-1} \Big)$$

$$\hat{\mathcal{V}}_x = \frac{1}{2} \Big(\hat{\mathcal{Q}}_{xx} - \hat{\mathcal{Q}}_{yy} \Big) = \begin{pmatrix} 0 & 0 & 1 \\ 0 & 0 & 0 \\ 1 & 0 & 0 \end{pmatrix} \qquad \hat{V}_x = \hat{a}_{+1}^\dagger \hat{a}_{-1} + \hat{a}_{-1}^\dagger \hat{a}_{+1}$$

$$\hat{\mathcal{V}}_y = \hat{\mathcal{Q}}_{xy} = \mathrm{i} \begin{pmatrix} 0 & 0 & -1 \\ 0 & 0 & 0 \\ 1 & 0 & 0 \end{pmatrix} \qquad \hat{V}_y = \mathrm{i} \hat{a}_{+1}^\dagger \hat{a}_{-1} - \mathrm{i} \hat{a}_{-1}^\dagger \hat{a}_{+1}$$

$$\hat{\mathcal{N}}^+ = \begin{pmatrix} 1 & 0 & 0 \\ 0 & 0 & 0 \\ 0 & 0 & 1 \end{pmatrix} \qquad \hat{N}^+ = \hat{a}_{+1}^\dagger \hat{a}_{+1} + \hat{a}_{-1}^\dagger \hat{a}_{-1}$$

A.2 Calculation for POVM Measurement

Each rotation in F=1 is generated by the Spin-1 operators. The coupling / storage pulses are given by the Pauli σ_x and σ_y matrices in a Spin-$\frac{1}{2}$ Hilbert subspace of the respective levels:

$$C_x^{ij} = \frac{1}{2}\begin{pmatrix} 0 & 1 \\ 1 & 0 \end{pmatrix} = \frac{1}{2}\left(a_{1,i}^\dagger a_{2,j} + a_{2,j}^\dagger a_{1,i}\right) \tag{A.1}$$

$$C_y^{ij} = \frac{1}{2}\begin{pmatrix} 0 & i \\ i & 0 \end{pmatrix} = \frac{i}{2}\left(a_{1,i}^\dagger a_{2,j} + a_{2,j}^\dagger a_{1,i}\right) \tag{A.2}$$

If one wants to calculate the whole rotation at once, it would be an $3 \oplus 5$ Hilbert space, so I chose to compute it one after the other by hand. Here is my "cheat-sheet" in second quantization:

$$\begin{aligned} S_x^2 &= \frac{1}{2}\left(a_0^\dagger a_1 + a_0^\dagger a_{-1} + a_1^\dagger a_0 + a_{-1}^\dagger a_0\right)^2 \\ &= \frac{1}{2}\left(2a_0^\dagger a_0 + a_1^\dagger a_1 + a_{-1}^\dagger a_{-1} + a_1^\dagger a_{-1} + a_{-1}^\dagger a_1\right) \end{aligned} \tag{A.3}$$

$$\begin{aligned} S_y^2 &= \frac{-1}{2}\left(a_0^\dagger a_1 - a_0^\dagger a_{-1} - a_1^\dagger a_0 + a_{-1}^\dagger a_0\right)^2 \\ &= \frac{1}{2}\left(2a_0^\dagger a_0 + a_1^\dagger a_1 + a_{-1}^\dagger a_{-1} - a_1^\dagger a_{-1} - a_{-1}^\dagger a_1\right) \end{aligned} \tag{A.4}$$

$$\mathrm{e}^{-i\varphi S_x} = \mathbb{I}_3 - S_x^2 + \cos(\varphi)S_x^2 - i\sin(\varphi)S_x \tag{A.5}$$

$$\mathrm{e}^{-i\varphi S_y} = \mathbb{I}_3 - S_y^2 + \cos(\varphi)S_y^2 - i\sin(\varphi)S_y \tag{A.6}$$

$$\mathrm{e}^{-i\varphi C_x^{ij}} = \cos(\varphi/2)\mathbb{I}_2^{ij} - i\sin(\varphi/2)\left[a_{1,i}^\dagger a_{2,j} + a_{2,j}^\dagger a_{1,i}\right] \tag{A.7}$$

$$\mathrm{e}^{-i\varphi C_y^{ij}} = \cos(\varphi/2)\mathbb{I}_2^{ij} + \sin(\varphi/2)\left[a_{1,i}^\dagger a_{2,j} - a_{2,j}^\dagger a_{1,i}\right] \tag{A.8}$$

$$\mathrm{e}^{-i\pi/2 S_x} = \frac{1}{2}\left(a_1^\dagger a_1 + a_{-1}^\dagger a_{-1} - a_1^\dagger a_{-1} - a_{-1}^\dagger a_1\right) - \frac{i}{\sqrt{2}}\left(a_0^\dagger a_1 + a_0^\dagger a_{-1} + a_1^\dagger a_0 + a_{-1}^\dagger a_0\right) \tag{A.9}$$

$$\mathrm{e}^{-i\pi/2 S_y} = \frac{1}{2}\left(a_1^\dagger a_1 + a_{-1}^\dagger a_{-1} + a_1^\dagger a_{-1} + a_{-1}^\dagger a_1\right) + \frac{1}{\sqrt{2}}\left(a_0^\dagger a_1 - a_0^\dagger a_{-1} - a_1^\dagger a_0 + a_{-1}^\dagger a_0\right) \tag{A.10}$$

$$\mathrm{e}^{-i3\pi/2 S_x} = \frac{1}{2}\left(a_1^\dagger a_1 + a_{-1}^\dagger a_{-1} - a_1^\dagger a_{-1} - a_{-1}^\dagger a_1\right) + \frac{i}{\sqrt{2}}\left(a_0^\dagger a_1 + a_0^\dagger a_{-1} + a_1^\dagger a_0 + a_{-1}^\dagger a_0\right) \tag{A.11}$$

$$\mathrm{e}^{-i3\pi/2 S_y} = \frac{1}{2}\left(a_1^\dagger a_1 + a_{-1}^\dagger a_{-1} + a_1^\dagger a_{-1} + a_{-1}^\dagger a_1\right) - \frac{1}{\sqrt{2}}\left(a_0^\dagger a_1 - a_0^\dagger a_{-1} - a_1^\dagger a_0 + a_{-1}^\dagger a_0\right) \tag{A.12}$$

$$\mathrm{e}^{-i\pi S_x} = -a_0^\dagger a_0 - a_1^\dagger a_{-1} - a_{-1}^\dagger a_1 \tag{A.13}$$

$$\mathrm{e}^{-i\pi S_y} = -a_0^\dagger a_0 + a_1^\dagger a_{-1} + a_{-1}^\dagger a_1 \tag{A.14}$$

A.3 Additional figures

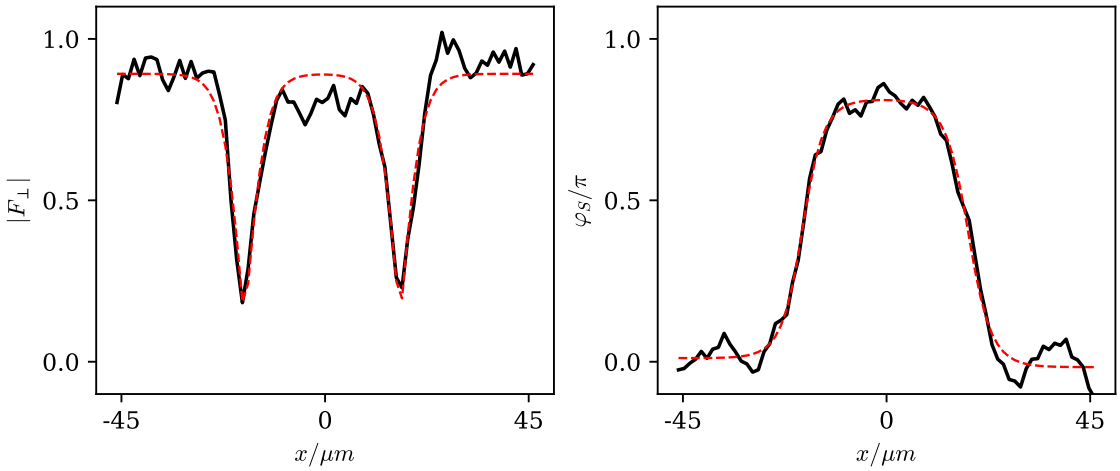

Figure A.1: K-$\bar{K}$ solition collision from the measurement with the DuPR. On the left is the $|F_\perp|$ profile shown with a fit from Eq. (4.1) in red, as an example for the complete velocity and phase shift extraction. On the right is the spinor phase profile of the same time slice drawn, with an equivalent fit from Eq. (2.44). The increase in noise is visible on the background, but the form of the solitons can clearly be extracted.

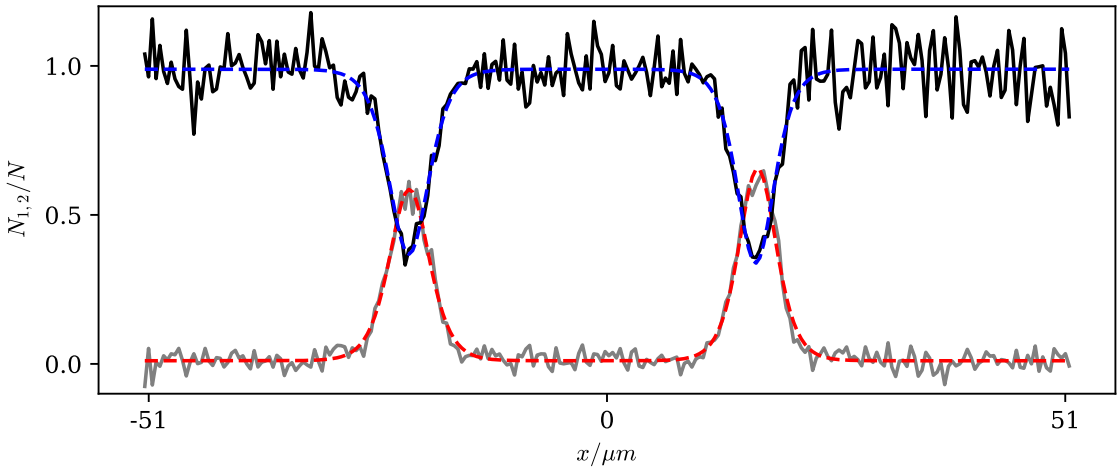

Figure A.2: Here, a time slice of the pseudospin-1/2 system is shown. In black is the population of $|F = 1, m_\mathrm{F} = 0\rangle$ with a fit of two dark solitions, in gray is the population of $|F = 2, m_\mathrm{F} = 0\rangle$ with a fit of two bright solitons drawn, following Eq. (4.3).

B Bibliography

[1] Mark J Ablowitz. *Nonlinear dispersive waves: asymptotic analysis and solitons*, volume 47. Cambridge University Press, 2011.

[2] Christoph Becker, Simon Stellmer, Parvis Soltan-Panahi, Sören Dörscher, Mathis Baumert, Eva-Maria Richter, Jochen Kronjäger, Kai Bongs, and Klaus Sengstock. Oscillations and interactions of dark and dark–bright solitons in bose–einstein condensates. *Nature Physics*, 4(6):496–501, 2008.

[3] David K. Campbell, Michel Peyrard, and Pasquale Sodano. Kink-antikink interactions in the double sine-gordon equation. *Physica D: Nonlinear Phenomena*, 19(2):165–205, 1986. ISSN 0167-2789. doi: https://doi.org/10.1016/0167-2789(86)90019-9. URL https://www.sciencedirect.com/science/article/pii/0167278986900199.

[4] Xiao Chai, Li You, and Chandra Raman. Magnetic solitons in an immiscible two-component bose-einstein condensate. *Phys. Rev. A*, 105:013313, Jan 2022. doi: 10.1103/PhysRevA.105.013313. URL https://link.aps.org/doi/10.1103/PhysRevA.105.013313.

[5] Jesús Cuevas-Maraver, Panayotis G. Kevrekidis, and Floyd Williams. *The sine-Gordon Model and it's Applications*. Springer Nature, Cambridge, England, 2014.

[6] Franco Dalfovo, Stefano Giorgini, Lev P Pitaevskii, and Sandro Stringari. Theory of bose-einstein condensation in trapped gases. *Reviews of modern physics*, 71(3):463, 1999.

[7] Yannick Deller, Alexander Schmutz, Raphael Schäfer, Alexander Flamm, Florian Schmitt, Ido Siovitz, Thomas Gasenzer, Panayotis G. Kevrekidis, Helmut Strobel, and Markus K. Oberthaler. Observation of sine-gordon solitons in a spinor bose-einstein condensate. submitted, 2025.

[8] Daniel Doering, Gordon McDonald, JE Debs, Cristina Figl, PA Altin, H-A Bachor, NP Robins, and JD Close. Quantum-projection-noise-limited interferometry with coherent atoms in a ramsey-type setup. *Physical Review A—Atomic, Molecular, and Optical Physics*, 81(4):043633, 2010.

[9] Steven T Flammia, Andrew Silberfarb, and Carlton M Caves. Minimal informationally complete measurements for pure states. *Foundations of Physics*, 35(12): 1985–2006, 2005.

[10] Murray Gell-Mann. Symmetries of baryons and mesons. *physical review*, 125(3): 1067–1084, 1962.

[11] D Gordon and CM Savage. Excitation spectrum and instability of a two-species bose-einstein condensate. *Physical Review A*, 58(2):1440, 1998.

[12] C. D. Hamley, C. S. Gerving, T. M. Hoang, E. M. Bookjans, and M. S. Chapman. Spin-nematic squeezed vacuum in a quantum gas. *Nature Physics*, 8(4):305–308, Apr 2012. ISSN 1745-2481. doi: 10.1038/nphys2245. URL https://doi.org/10.1038/nphys2245.

[13] Chris D Hamley, CS Gerving, Thai M Hoang, Eva M Bookjans, and Michael S Chapman. Spin-nematic squeezed vacuum in a quantum gas. *Nature Physics*, 8(4): 305–308, 2012.

[14] Serge Haroche and J-M Raimond. *Exploring the quantum: atoms, cavities, and photons*. Oxford university press, 2006.

[15] Carl W Helstrom. Cramer-rao inequalities for operator-valued measures in quantum mechanics. *International Journal of Theoretical Physics*, 8(5):361–376, 1973.

[16] Pascual Jordan. Der Zusammenhang der symmetrischen und linearen Gruppen und das Mehrkörperproblem. *Zeitschrift füer Physik*, 94:531–535, Mar 1935.

[17] Yuri S Kivshar and Boris A Malomed. Dynamics of solitons in nearly integrable systems. *Reviews of Modern Physics*, 61(4):763, 1989.

[18] Felix Maximilian Klein. Nonlinear spin dynamics initiated by local control of the spinor phase in a bose-einstein condensate. Master's thesis, Ruperto-Carola-University of Heidelberg, 2024.

[19] G Kleine Büning, J Will, Wolfgang Ertmer, E Rasel, Jan Arlt, Carsten Klempt, Fernando Ramírez-Martínez, F Piéchon, and Peter Rosenbusch. Extended coherence time on the clock transition of optically trapped rubidium. *Physical review letters*, 106(24):240801, 2011.

[20] Rebekka Koch and Alvise Bastianello. Exact thermodynamics and transport in the classical sine-Gordon model. *SciPost Phys.*, 15:140, 2023. doi: 10.21468/SciPostPhys.15.4.140. URL https://scipost.org/10.21468/SciPostPhys.15.4.140.

[21] Philipp Kunkel. *Splitting a Bose-Einstein condensate enables EPR steering and simultaneous readout of noncommuting observables*. PhD thesis, Ruperto-Carola-University of Heidelberg, 2019.

[22] Philipp Kunkel, Maximilian Prüfer, Stefan Lannig, Rodrigo Rosa-Medina, Alexis Bonnin, Martin Gärttner, Helmut Strobel, and Markus K. Oberthaler. Simultaneous readout of noncommuting collective spin observables beyond the standard quantum limit. *Phys. Rev. Lett.*, 123:063603, Aug 2019. doi: 10.1103/PhysRevLett.123.063603. URL https://link.aps.org/doi/10.1103/PhysRevLett.123.063603.

[23] Stefan Lannig. *Vector Solitons and Different Scenarios of Universal Dynamics in a Spin-1 Bose-Einstein Condensate*. PhD thesis, Ruperto-Carola-University of Heidelberg, 2022.

[24] Stefan Lannig, Christian-Marcel Schmied, Maximilian Prüfer, Philipp Kunkel, Robin Strohmaier, Helmut Strobel, Thomas Gasenzer, Panayotis G. Kevrekidis, and Markus K. Oberthaler. Collisions of three-component vector solitons in bose-einstein

condensates. *Phys. Rev. Lett.*, 125:170401, Oct 2020. doi: 10.1103/PhysRevLett.125.170401. URL https://link.aps.org/doi/10.1103/PhysRevLett.125.170401.

[25] Harry Levine, Dolev Bluvstein, Alexander Keesling, Tout T Wang, Sepehr Ebadi, Giulia Semeghini, Ahmed Omran, Markus Greiner, Vladan Vuletić, and Mikhail D Lukin. Dispersive optical systems for scalable raman driving of hyperfine qubits. *Physical Review A*, 105(3):032618, 2022.

[26] Robert McLachlan. A gallery of constant-negative-curvature surfaces. *Mathematical Intelligencer*, 16(4), 1994.

[27] KM Mertes, JW Merrill, R Carretero-González, DJ Frantzeskakis, PG Kevrekidis, and DS Hall. Nonequilibrium dynamics and superfluid ring excitations in binary bose-einstein condensates. *Physical review letters*, 99(19):190402, 2007.

[28] E Nicklas, H Strobel, T Zibold, C Gross, BA Malomed, PG Kevrekidis, and MK Oberthaler. Rabi flopping induces spatial demixing dynamics. *Physical Review Letters*, 107(19):193001, 2011.

[29] Michael A. Nielsen and Isaac L. Chuang. *Quantum Computation and Quantum Information: 10th Anniversary Edition*. Cambridge University Press, 2010.

[30] Lev Pitaevskii and Sandro Stringari. *Bose-Einstein Condensation and Superfluidity*. Oxford University Press, 2016.

[31] Maximilian Prüfer. *Experimental testing quantum field theory concepts with spinor Bose gases far from equilibrium*. PhD thesis, Ruperto-Carola-University of Heidelberg, 2020.

[32] Maximilian Prüfer, Daniel Spitz, Stefan Lannig, Helmut Strobel, Jürgen Berges, and Markus K. Oberthaler. Condensation and thermalization of an easy-plane ferromagnet in a spinor bose gas. *Nature Physics*, 18:1459, Dez 2022. ISSN 1745-2481. doi: 10.1038/s41567-022-01779-6. URL https://doi.org/10.1038/s41567-022-01779-6.

[33] Chunlei Qu, Lev P. Pitaevskii, and Sandro Stringari. Magnetic solitons in a binary bose-einstein condensate. *Phys. Rev. Lett.*, 116:160402, Apr 2016. doi: 10.1103/PhysRevLett.116.160402. URL https://link.aps.org/doi/10.1103/PhysRevLett.116.160402.

[34] J Rogel-Salazar, S Choi, G H C New, and K Burnett. Methods of quantum field theory for trapped bose–einstein condensates. *Journal of Optics B: Quantum and Semiclassical Optics*, 6(9):R33, jun 2004. doi: 10.1088/1464-4266/6/9/R01. URL https://doi.org/10.1088/1464-4266/6/9/R01.

[35] Julian Schwinger. Angular momentum. In *Quantum Mechanics: Symbolism of Atomic Measurements*, pages 149–181. Springer, 1952.

[36] Prashant Singh and K Senthilnathan. Evolution of a solitary wave: optical soliton, soliton molecule and soliton crystal. *Discover Applied Sciences*, 6(9):464, 2024.

[37] Ido Siovitz, Anna-Maria E. Glück, Yannick Deller, Alexander Schmutz, Felix Klein, Helmut Strobel, Markus K. Oberthaler, and Thomas Gasenzer. Double sine-gordon class of universal coarsening dynamics in a spin-1 bose gas. *Phys. Rev. A*, 112: 023304, Aug 2025. doi: 10.1103/df5w-3yfd. URL https://link.aps.org/doi/10.1103/df5w-3yfd.

[38] H Sosa-Martinez, NK Lysne, CH Baldwin, A Kalev, IH Deutsch, and PS Jessen. Experimental study of optimal measurements for quantum state tomography. *Physical Review Letters*, 119(15):150401, 2017.

[39] Dan M Stamper-Kurn and Masahito Ueda. Spinor bose gases: Symmetries, magnetism, and quantum dynamics. *Reviews of Modern Physics*, 85(3):1191–1244, 2013.

[40] Daniel A Steck. Rubidium 87 d line data. http://steck.us/alkalidata, 2001. revision 2.3.4, 8. August 2025.

[41] Helmut Strobel. *Fisher Information and entanglement of non-Gaussian spin states*. PhD thesis, Ruperto-Carola-University of Heidelberg, 2015.

[42] Levi Suelberg. A sagnac interferometer setup for local microwave-transition in a spinor 87rb bose-einstein condensate. Bachelorarbeit, Universität Heidelberg, 2025.

[43] Elisabeth Wybo, Alvise Bastianello, Monika Aidelsburger, Immanuel Bloch, and Michael Knap. Preparing and analyzing solitons in the sine-gordon model with quantum gas microscopes. *PRX Quantum*, 4(3):030308, 2023.

[44] Xiaoquan Yu and P. B. Blakie. Dark-soliton-like magnetic domain walls in a two-dimensional ferromagnetic superfluid. *Phys. Rev. Res.*, 3:023043, Apr 2021. doi: 10.1103/PhysRevResearch.3.023043. URL https://link.aps.org/doi/10.1103/PhysRevResearch.3.023043.

Erklärung:

Ich versichere, dass ich diese Arbeit selbstständig verfasst habe und keine anderen als die angegebenen Quellen und Hilfsmittel benutzt habe.

Heidelberg, den 6. November 2025 .....